Optimizing Mixer Geometries for Dielectrophoretic Micro-concentrators

by

Hsu-Yi Lee
Bachelor of Science, Mechanical Engineering
National Taiwan University, 2003

Submitted to the Department of Electrical Engineering and Computer Science
in Partial Fulfillment of the Requirements for the Degree of

Master of Science
at the
Massachusetts Institute of Technology

May 23, 2006

Author: _____
Department of Electrical Engineering and Computer Science
May 23, 2006

Certified by: _____
Joel Voldman
Thesis Supervisor

Accepted by: _____
Arthur C. Smith
Chairman, Department Committee on Graduate Theses

Optimizing Mixer Geometries for Dielectrophoretic Micro-concentrators

By

Hsu-Yi Lee

Submitted to the
Department of Electrical Engineering and Computer Science

May 23, 2006

in Partial Fulfillment of the Requirements for the Degree of
Master of Science

ABSTRACT

Dielectrophoretic (DEP) force, generated by interdigitated electrodes (IDEs), has been utilized to capture bio-particles for microfluidic concentration. However, due to the localized DEP force, DEP-based μ -concentrators usually have shallow channels and thus are operated under low flow rates. In this thesis, we propose a mixer-enhanced DEP-based concentrator which can be operate under high flow rates (~200 μl/min) with 20 V_{pp} applied voltage. In particular, the optimal geometries of micromixers for the device are investigated and determined by simulations and experiments. The optimal micromixer-enhanced concentrator exhibits up to 1.5 × improvement in trapping efficiency as compared to a concentrator without mixers.

Thesis Supervisor: Joel Voldman
Title: NBX Assistant Professor of Electrical Engineering and Computer Science

ACKNOWLEDGEMENTS

I would like to use my limited vocabulary to acknowledge and thank all of the people who have helped me with this work. First and foremost, I would like to thank my advisor, Prof. Joel Voldman, not only for always providing insight, guidance, and support in research, but also for bringing an optimistic and cheerful attitude to life. Without his help, I would never survive my first year in MIT, not mention finishing my Master's thesis with such an optimistic outlook.

I would also like to thank all my labmates in Voldman's group, for always being so friendly and so generous with giving me help either in research or in life. I owe special thanks to Salil Desai, for his time and effort on maintaining the server and solving all the troublesome problems. Without his help, I could not have done my simulations so smoothly. I also want to give a big thanks to Michael Vahey, for always being willing to answer all my questions with his intelligence and for being encouraging all the time as well. Thanks to Brian, not only for sharing his simulation and fabrication skills, but also for providing the cheerful cynicism towards everything. To Lily and Katya, thanks for being such considerate officemates and always give me the best advice. To Adam, thanks for always being generous and spending time discussing different things with me. I would also like to give thanks to Joseph for the solidarity though the nasty SU-8 process; to Nick and Pat, for always bring new ideas and suggestions from different points of view. While already graduated, I would like to thank Nitzan, for developing the fabrication process that I could easily start with.

Outside of the lab, I would like to thank the MTL staff, especially Dennis Ward. He taught me how to do the SU-8 process and his cheerful presence made the cleanroom much more bearable.

I also owe many thanks to my boyfriend Kevin, for always being supportive and tolerant, especially when I was stressed out. And last but certainly not least, to my family, especially my parents, thanks for encouraging and supporting me to study aboard; even though they are far way from the US, their caring support never changes.

TABLE OF CONTENTS

CHAPTER 1: INTRODUCTION **8**

1.1 BACKGROUND 8
1.2 DEVICE OVERVIEW 15
1.3 THESIS SCOPE 16

CHAPTER 2: MODELING AND DESIGN **17**

2.1 FLUIDIC AND ELECTRIC FIELDS 17
2.1.1 Fluid Flow Field *17*
2.1.2 Electric Field *19*
2.2 MODELING FORCES AND PARTICLE MOTION 20
2.2.1 Particle Properties *20*
2.2.2 DEP Force *21*
2.2.3 Drag Force *21*
2.2.4 Gravitational Forces *23*
2.2.5 Rigid Substrate and Wall Forces *23*
2.2.6 Particle Motion and Tracking *25*
2.3 FLUIDIC FIELD VERIFICATION 26
2.4 DESIGN 28
2.4.1 Electrode Width and Spacing *28*
2.4.2 Mixer Geometry *29*

CHAPTER 3: MICROFABRICATION AND PACKAGING **32**

3.1 MASKS 32
3.1.1 Electrode Mask *32*
3.1.2 SU-8 Mask *33*
3.2 MICROFABRICATION 35
3.2.1 Au Electrode *35*
3.2.2 SU-8 Mold and PDMS Micromixer *37*
3.3 PACKAGING 40
3.3.1 Printed Circuit Board *40*
3.3.2 Assembly *41*

CHAPTER 4: DEVICE TESTING **43**

4.1 MATERIALS AND TOOLS 43
4.1.1 Test Particles *43*
4.1.2 Test Setup *44*
4.2 MEASUREMENT METHOD 45
4.2.1 Image Processing Algorithm *46*
4.2.2 Image Processing Validation *49*
4.3 EXPERIMENT 50

CHAPTER 5: RESULT **53**

5.1 TRAPPED PARTICLE DISTRIBUTION 53
5.1.1 Qualitative Results *53*
5.1.2 Quantitative Results *56*
5.2 TRAPPING ENHANCEMENT 57
5.3 COMBINATION OF MIXERS 59

CHAPTER 6: CHALLENGES AND FUTURE WORK **61**

6.1 SIMULATION 61
6.1.1 Resolution for DEP Modeling *61*

6.1.2 Shielding Effect *62*
6.2 MIXER OPTIMIZATION 63
6.3 FABRICATION 64
6.4 TESTING 65
6.5 CONTRIBUTIONS 66
APPENDIX: FABRICATION PROCESS FLOW **67**
REFERENCES **69**

LIST OF FIGURES

FIGURE 1-1: DIELECTROPHORESIS 9
FIGURE 1-2: MAXIMUM FLOW RATE VERSUS CROSS SECTION ASPECT RATIO 11
FIGURE 1-3: MAGNITUDE OF THE DEP FORCE ABOVE IDES 12
FIGURE 1-4: PARTICLE TRAPPING ENHANCEMENT BY MICROMIXER 12
FIGURE 1-5: CLASSIFICATION SCHEME FOR MICROMIXERS 14
FIGURE 1-6: DEVICE OVERVIEW 15
FIGURE 2-1: GEOMETRY OF THE PERIODIC UNIT OF THREE MICROMIXERS. 18
FIGURE 2-2: ELECTRIC FIELD STREAMLINES 19
FIGURE 2-3: ILLUSTRATION OF THE FORCES ON A PARTICLE 20
FIGURE 2-4: VELOCITY VECTOR PLOT 23
FIGURE 2-5: PARTICLE MOTION CORRESPONDING TO WALL FORCE 24
FIGURE 2-6: TRAJECTORIES OF PARTICLES IN SHM 25
FIGURE 2-7: VISUALIZATION OF THE SHM MIXING PATTERN (FROM THE 1ST TO 3RD PERIOD) 26
FIGURE 2-8: VISUALIZATION OF THE SGM MIXING PATTERN (FROM THE 1ST TO 3RD PERIOD) 27
FIGURE 2-9: CONTOUR PLOT OF LOGARITHMIC DEP FORCE 28
FIGURE 2-10: TRAJECTORY PLOTS 30
FIGURE 2-11: MIXER DIMENSION 31
FIGURE 3-1: ELECTRODE MASK 33
FIGURE 3-2: MICROMIXER MASK 34
FIGURE 3-3: GOLD LIFTOFF PROCESS 36
FIGURE 3-4: GOLD INTERDIGITATED ELECTRODES 37
FIGURE 3-5: SU-8 STRUCTURE AND PDMS MICROMIXER FABRICATION PROCESS 38
FIGURE 3-6: PDMS MICROMIXER 39
FIGURE 3-7: PCB LAYOUT AND PACKAGED DEVICE 40
FIGURE 4-1: EXPERIMENTAL SETUP 44
FIGURE 4-2: INTENSITY TO CONCENTRATION CALIBRATION 46
FIGURE 4-3: BINARY IMAGE CONVERSION 48
FIGURE 4-4: EXPERIMENTAL CALIBRATION WITH BINARY ALGORITHM 50
FIGURE 4-5: MEASUREMENT PROCESS FOR DEVICE CHARACTERIZATION 51
FIGURE 5-1: THE STABILITY OF THE TRAPPING RESULT VERSUS THE NUMBER OF STARTING PARTICLES 54
FIGURE 5-2: PARTICLE DISTRIBUTION AND FLOW STREAMS 55
FIGURE 5-3: MICROSCOPE PHOTOGRAPHS OF THE TRAPPED BEAD DISTRIBUTION ALONG THE CHANNEL 56
FIGURE 5-4: EXPERIMENTAL TRAPPED BEAD NUMBER ALONG THE CHANNEL LENGTH 57
FIGURE 5-5: EXPERIMENTAL TRAPPING EFFICIENCY WITH VARYING INPUT CONCENTRATION 58
FIGURE 5-6: COMPARISON OF SIMULATION AND EXPERIMENTAL TRAPPING EFFICIENCY 59
FIGURE 5-7: COMBINATIONAL MIXER PERFORMANCE 60
FIGURE 6-1: PLOT OF Z-DIRECTED DEP FORCE 62
FIGURE 6-2: LENGTH OF SGM TO COMPLETE ONE CIRCULATION 64

LIST OF TABLES

TABLE 1:CHANNEL DIMENSIONS BASED ON MIXER PUBLICATIONS 31

Chapter 1: Introduction

1.1 Background

Rapid, highly-sensitive detection and genetic analysis of pathogens still remains as one of the most important goals of biotechnology. The applications of pathogen detection are essential to homeland security, public health, veterinary diagnostics, and others. Polymerase chain reaction (PCR) [1] is one of the commonly used methods because of its potential for detecting a specific gene in a complex sample when there are less than 10 copies available. However, a PCR-based detection system still can not address a number of challenges while sampling complex substrates even though it is potentially sensitive. For example, when PCR is used to detect pathogens in water, the impurities in the water can reduce the sensitivity of the assay and interfere with the analysis. If sampling conditions have an adverse impact on the assay, the system may fail to detect a given pathogen in a small amount of concentrated liquid that is known to present a health risk. To improve the accuracy of pathogen detection, pre-concentration and purification of a sample are necessary. Besides, samples are often collected on a milliliter scale, whereas most pathogen-detecting devices can only process samples on a microliter scale in a reasonable span of time. Thus, using a pre-concentrator is a must because it not only cuts down the volume of the sample but also keeps the pathogens we want to analyze.

While seeking suitable techniques, my group and I have reached an agreement that we need a method which can be integrated with the Total Analysis Systems (μTAS) or Lab-on-a-Chip (LOC)—the micro systems which are now becoming a new focus for biomedical analyses. The goal of μTAS and LOC is to fully integrate the necessary functions into a micro-analytical system which can perform complete analysis cycles on the same microdevice. These types of devices offer the potential for highly efficient, simultaneous analysis of a large number of biologically important molecules in genomic, proteomic, and metabolic studies. Some general review papers [2-4] on μTAS have mentioned a number of sample pre-concentration methods that are compatible with a μTAS system, such as field-amplified sample stacking [5], ultrafiltration membranes [6],

zone electrophoresis (ZE), iso-electric focusing (IEF) [7], and dielectrophoresis (DEP) [8, 9].

Among these methods, dielectrophoresis has captured our attention due to its ability to effectively trap, manipulate, and separate particles ranging from large DNA strands [10] to cells and bacteria [8] in microfabricated devices. Dielectrophoresis describes the motion of particles caused by dielectric polarization effects in a non-uniform electric field. Polarized particles in the non-uniform field result in different forces on each side (Figure 1-1). Thus, depending on the relative polarizability of a particle with respect to its surrounding medium, the particle will be induced to move either towards the high-electric-field region (positive DEP, Figure 1-1a) or towards the weak-electric-field region (negative DEP, Figure 1-1b). Based on DEP strength, two

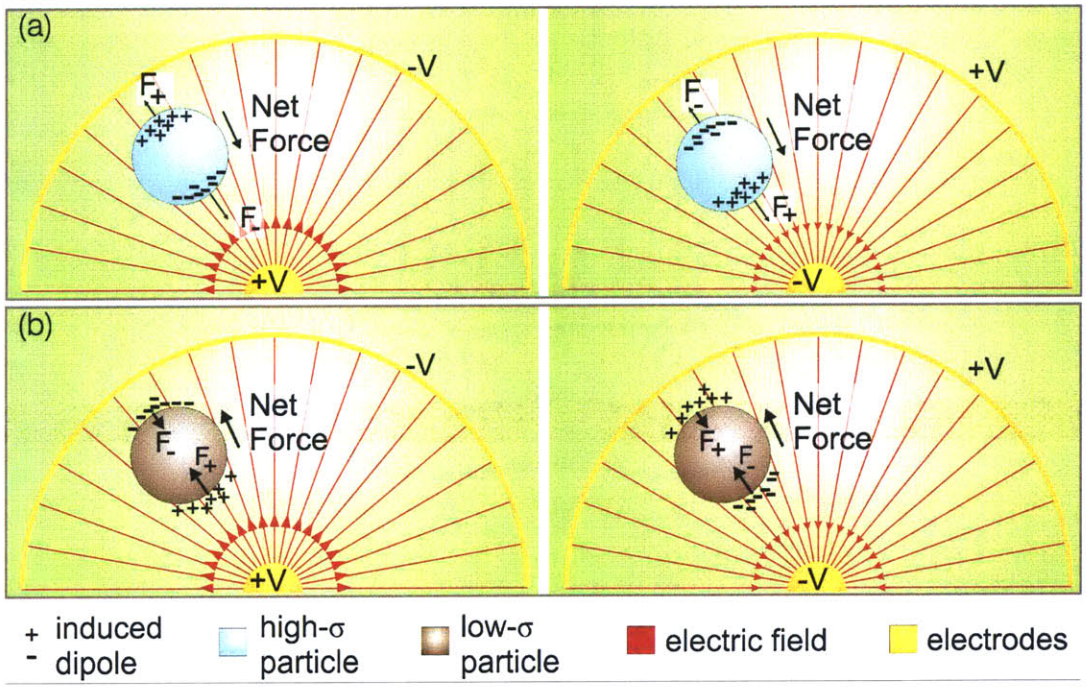

Figure 1-1: Dielectrophoresis

A particle is exposed to a non-uniform electric field generated by electrodes of spherical geometry. (a) Positive dielectrophoresis: the particle is more polarizable than the surrounding medium, and the net force draws the particle toward the maximum electric field. (b) Negative dielectrophoresis: the particle is less polarizable than the surrounding medium, and the net force pushes the particle toward the minimum electric field.

main operations are used to concentrate particles. In the first operation, the DEP dominates diffusion but does not overcome the flow, so the particles remain mobile in the flow but the direction of motion is altered by the DEP force. By exclusively collecting the section in the stream where the particles have been moved to by the DEP force, concentration can be achieved [11]. In the second operation, the DEP overcomes diffusion and the flow, so particles are immobilized in the highest/lowest electric field region and are concentrated there. This operation has been utilized more often in μ-concentrators because the resulting concentration can be close to solid density.

The non-uniformity of the electric field can be produced either by an array of insulating posts [12, 13] , glass beads [14], or metal electrodes [15-17]. For the insulating posts and glass beads, they themselves become obstacles in the electric field, so the electric field streams have to detour around them, and thus the electric field gradients will be produced. In those designs, the electric field (~50 V/mm) is generated across the channel (~10 mm) between two electrodes, so a high-voltage power supply (>500 V_{pp}) is required. On the other hand, an array of electrodes can generate a non-uniform electric field in the micron scale gaps between the electrodes. As the gap is small, a reasonable voltage (~20 V_{pp}) is enough to generate a sufficient electric field. Among the type of electrodes, interdigitated electrodes (IDE) are widely used because they are easy to fabricate and an analytical electrical field solution exists for modeling.

Several concentrators with IDE arrays have been presented and have demonstrated particle trapping results [10, 15, 18]. However, the maximum flow velocity in the channels of those devices is limited by the maximum DEP trapping force capable with the IDEs, so these devices have to be operated at low flow rates (<1 μl/min). To achieve a higher flow rate without increasing the maximum flow velocity in the channel, the cross section of the channel needs to be enlarged in width and height. In particular, with the same cross section area and same applied voltage, IDEs in a higher height-to-width aspect ratio channel can hold particles against faster flow rates (Figure 1-2).

However, it is known that the magnitude of the DEP force reduces quickly with distance above the electrodes (Figure 1-3). As the channel height increases, the particles in the channel which are higher than the DEP effective region will not experience the DEP force and will therefore not be trapped (Figure 1-4a). For example, under 300

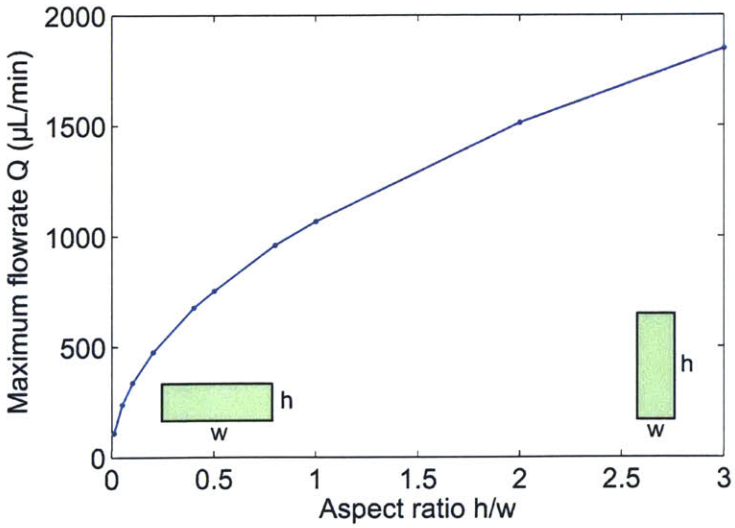

Figure 1-2: Maximum flow rate versus cross section aspect ratio

The maximum flow rate that electrodes can hold particles against is calculated under the conditions: applied voltage 20 V_{pp}, electrode width and spacing 20 μm, cross section area 1e5 μm^2, particle diameter 1 μm, CM factor 0.8, and media density 1000 kg/m^3.

μl/min flow rate in a 500 μm width, 200 μm height channel, using 10 μm IDEs and 20 V_{pp} applied voltage can only capture pathogens which are 20~30 μm away within a reasonable channel length (~4 cm). To enhance particle trapping, complex flow is needed in the channel to circulate the particles so that more particles will be brought closer to the IDEs and become trapped (Figure 1-4b). Micromixers are one kind of component which is capable of circulating flow and feasible to be integrated in μ-concentrator. A micromixer enhanced DEP-based concentrator has been presented in [9], and it exhibited a 2~3x trapping enhancement before the electrodes saturated.

Employing micromixers to create complex flow has several advantages. First, micromixers have already been widely investigated because of the requirement of rapid mixing in many microfluidic systems for biological applications. Due to the low Renolds number in microfluidic systems, the pressure flows are laminar so the mixing of material between streams in flow is purely diffusive. The diffusive mixing is slow compared with the convection of material along the channel (i.e. large Péclet number, Pe>100). To increase the reaction or evenly distribute chemicals in biological processes such as cell

activation, enzyme reactions and protein folding mixing of reactants is required. Second, the fabrication of micromixers was based on technologies of micro electromechanical systems (MEMS) or polymeric fabrication techniques. They can either work as stand-alone devices or be integrated in a microfluidic system such as a μ-concentrator.

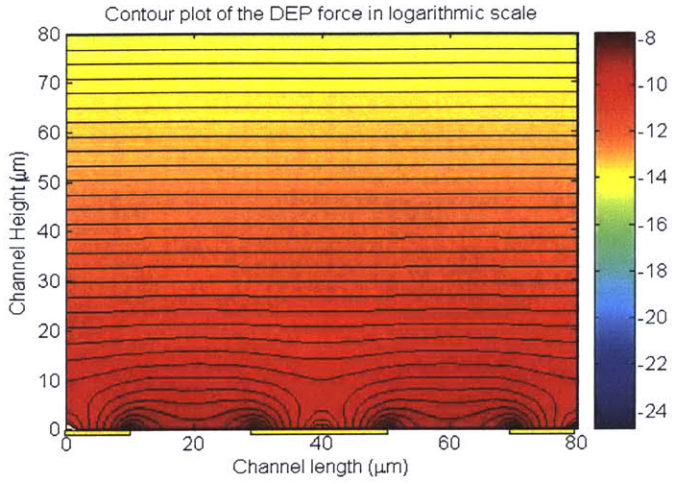

Figure 1-3: Magnitude of the DEP force above IDEs

The peaks of the DEP force occur at the edges of electrodes and the magnitude of the DEP force decays away from the electrodes. The electrode width and spacing in this case are 20 μm. Note the magnitude of the DEP force is expressed in logarithmic scale.

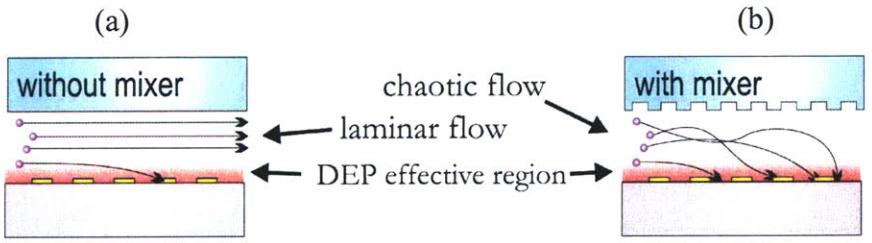

Figure 1-4: Particle trapping enhancement by micromixer

The interdigitated electrodes lining the bottom generate a DEP effective region (red region) where the particle will be trapped upon entering the channel. (a) In the smooth channel, only a portion of particles carried by laminar flow are exposed to DEP. (b) Chaotic flow generated by the passive micromixer on the top circulates more particles to the electrodes.

State-of-the-art micromixers can be categorized either as passive micromixers or as active micromixers (Figure 1-5) according to the ways that they generate disturbance. To achieve fast mixing, disturbance is necessary and can be generated by active components (such as a pump, valve, or electrode) which are often complicated in structure and require external energy. It is thus a challenge to integrate such an active micromixer into a microfluidic system. However, a passive micromixer does not require any external energy except a pressure difference to drive the flow. The fast mixing in a passive micromixer is usually achieved either by increasing the contact surface between different fluids to enhance molecular diffusion or by generating chaotic advection to fold two fluids. The mechanisms of chaotic advection are suitable for circulating the particles in the channel with IDE arrays. When the chaotic mixer is splitting, stretching, and folding the fluids, more particles moving along with the flow streams will be exposed to the DEP effective region (Figure 1-4b). At low Reynolds numbers (<100), chaotic advection can be generated by a modified channel structure such as a Tesla structure[19], serpentine structure[20], helix element [21] or other complex twisting shapes [22]. However, those structures with complicated 3-D geometries can result in difficult fabrication and device integration. In 2002, Johnson *et al* [23] investigated an alternative way of creating chaotic advection by placing a series of slanted grooves on the wall of the channel at an oblique angle. Almost at the same time, Stroock *et al* [24] published their results of two different groove mixers: the so-called slanted groove mixer (SGM) and the staggered herringbone mixer (SHM). These mixers can be fabricated through photolithographic processes just in two steps, and they can achieve uniform mixing (concentration standard deviation < 0.1) with short mixing lengths (~1cm). Due to the ease of fabrication and efficient mixing ability, patterned-groove mixers are the most suitable component to integrate with a concentrator containing IDE arrays.

In general, micromixers are designed toward achieving rapid and even mixing. The mixing performance is evaluated by the degree of uniform mixing in a fixed mixing length and the length for complete mixing. The degree of uniform mixing can be represented by the entropy of particle distribution [25], the heterogeneity of the distribution of tracers [26], or the standard deviation of the particle concentration [24]. The length of complete mixing is the length where the mixing entropy reaches the

maximum, or the heterogeneity and the standard deviation go to zero. A good micromixer should mix heterogeneous liquids to high uniformity in a short mixing length. However, the criteria used to judge a micromixer for enhancing DEP-based trapping and achieving complete mixing are different. Since the purpose of the mixer is to aid DEP-based concentration, the optimal micromixer for concentrators with IDE arrays is not necessarily the micromixer with the best mixing performance. Instead, the most important function of the mixer is to aid in moving particles closer to the IDE arrays.

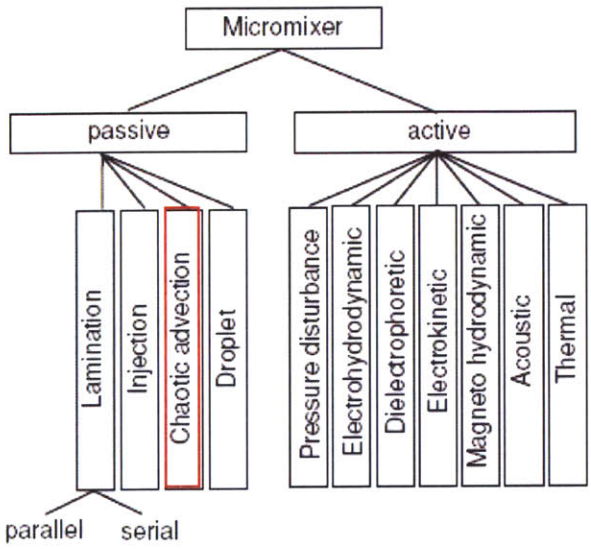

Figure 1-5: Classification scheme for micromixers

Micromixers can be categorized into two main groups: passive and active, according to the ways in which they generate disturbance. The scheme is reproduced from [27].

While the mixing efficiency is well-characterized either experimentally [24] or numerically [28-32], the effect of mixers on DEP-based concentrators has not been greatly explored. Therefore, the purpose of this work is to characterize and optimize mixer-enhanced μ-concentrators and not just mixers. I will accomplish this by first developing a modeling system which can simulate the particle motion in different mixer geometries. I will use the simulation result to design the optimal groove patterns which provide particle motion suitable for use with IDE arrays. Second I will fabricate the designed micromixer-enhanced μ-concentrator with standard MEMS technologies. Third, I will perform experiments on the fabricated device and establish a method to quantify

the trapping performance of the device. Fourth, to determine the optimal micromixer and verify the simulation, I will analyze the experiment data and compare them with the simulation predictions.

1.2 Device Overview

The device contains two major components: interdigitated electrodes and a micromixer, as illustrated in. On the bottom, the interdigitated electrodes generate positive DEP to collect particles in the passing flow. On the top, the micromixer—a flow channel with grooves—circulates the flow to expose more particles to the DEP effective region. When the IDEs have trapped enough particles, the DEP force can be deactivated, and the trapped particles can be released into a suspension of small volume, producing a concentrated sample. Evaluation of the concentration can be performed on-chip by making optical observations or off-chip by measuring the output sample with a spectrometer.

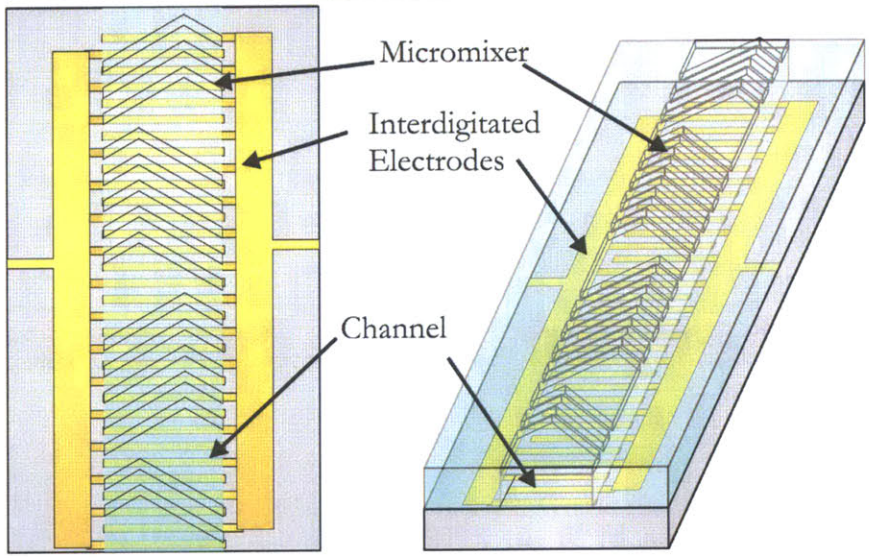

Figure 1-6: Device overview

The device consists of two major components: interdigitated electrodes and a micromixer. The flow channel is defined and enclosed by the micromixer. The particle suspension flowing into the channel is circulated by the micromixer on the top and trapped by the substrate on the interdigitated electrodes.

The micromixer is detachable from the device, so the same set of interdigitated electrodes can be used repeatedly with different micromixers. By using the same electrode arrays, the changes in electrical deviations due to fabrication inconsistencies are eliminated during the characterization of different mixers.

1.3 Thesis Scope

In this thesis, I present the characterization and optimization of different micromixers for DEP-based microorganism concentration. I first describe the force modeling and particle trapping simulations in Chapter 2 and then outline the device fabrication and packaging process in Chapter 3. In Chapter 4, I explain the experiment setup and the measurement algorithms for determining concentrations. I present the results of the simulations and experiments in Chapter 5 and discuss the challenges and possible improvements to this work in Chapter 6. Chapter 7 contains my conclusions.

Chapter 2: Modeling and Design

To characterize and optimize micromixers for the μ-concentrator, I developed a modeling environment that can simulate the particle motion in mixer-enhanced μ-concentrators. By simulating the particle motion, I can predict whether a particle is trapped by the electrodes in a given flow field and determine the trapping efficiency accordingly. The modeling environment took flow velocity, electric field and particle properties as the input. From these variables, it calculated the force fields and resulting particle movement. Using this modeling tool, I can predict the particle circulation and collection corresponding to the effect of mixers and electrodes of any arbitrary dimension and design the optimal device for particle concentration. In this chapter, I describe the calculation of the flow velocity and electric field and the modeling of forces exerted on particles. Then I describe the verification of the modeling tool and the design of the geometry of the micromixers and dimensions of the electrodes.

2.1 Fluidic and Electric Fields

Prior to modeling the force, I calculated the fluid flow field and electric field produced by micromixers and interdigitated electrodes, respectively. I used the fluid flow field and electric field later for modeling the hydrodynamic drag force and DEP force, respectively.

2.1.1 Fluid Flow Field

Due to the geometrical complexity of the grooves, no exact analytical solution for the flow in a chaotic micromixer is accessible. Therefore, numerical scheme is necessary for solving the fluid flow field. I used COMSOL Multiphysics as a numerical simulation tool to solve the flow velocity in the micromixer. To create and solve the model in COMSOL Multiphysics, I first drew a 3-D geometry of the mixer (Figure 2-1). Three kinds of groove geometry were used: slanted groove (SGM), normal herringbone (HM), staggered herringbone (SHM). Slanted groove and normal herringbone are for creating order flow by the symmetric geometry. Staggered herringbone is for creating chaotic flow by asymmetric geometry. I also drew and simulated a smooth channel without

grooves on the top as a simulation control. Since the micromixer geometry is not uniform in any dimension, the model can not be simplified to 2-D and thus a 3-D model is necessary. Due to the limitation of memory and the consideration of efficiency, the model only included 12 grooves, which is equivalent to 1 mixing period. I imposed pressure boundary conditions at the inlet and outlet and "no slip" elsewhere. I ran the simulation, using one arbitrary set of pressures (~100 Pa), and extrapolated to other pressures by scaling the fluidic field, using the linearity of the fluidic field with pressure.

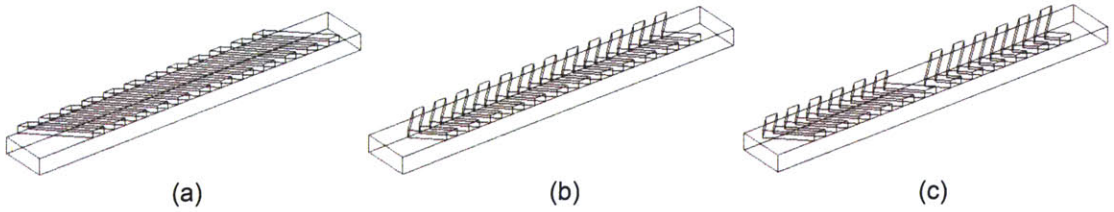

Figure 2-1: Geometry of the periodic unit of three micromixers.

(a) Slanted groove micromixer (SGM). (b) Herringbone micromixer (HM). (c) Staggered herringbone micromixer (SHM). Each periodic unit includes 12 ridges.

To generate the finite element mesh, I utilized the built-in mesh generators in COMSOL Multiphysics which can create a tetrahedral mesh automatically and the mesh can be refined manually when strict accuracy is required. The mesh size in COMSOL Multiphysics is defined as the ratio of the mesh length to the model length. I used the 1e-5 mesh size which is relatively coarser than the ones used in other published work. However, I observed that 1e-3 to 1e-5 mesh-size models provided very similar solutions, so I believe the solution is convergent and acceptable.

COMSOL Multiphysics then numerically solved the incompressible Navier-Strokes equations:

$$\rho\frac{\partial u}{\partial t}+\rho(u\cdot\nabla)u=\nabla\cdot[-pI+\eta(\nabla u+(\nabla u)^T)]+F \qquad \textbf{(2-1)}$$

$$\nabla\cdot u=0 \qquad \textbf{(2-2)}$$

where ρ is the fluid density, u is the flow velocity, η is the fluid dynamic viscosity, and F is the volume force. The media used in the simulation is water, so ρ is 1e3 kg/m and η is 1e-3 Pa·s. To visualize the results such as flow velocity and streamlines, I used the postprocessing function in COMSOL Multiphysics. A full mixer flow profile can be formed later by cascading the solution of one period in Matlab.

2.1.2 Electric Field

The interdigitated electrode lining at the bottom of the device generated an electric field. In order to derive this periodic and non-uniform electric field, I chose the closed-form analytic solution derived by Chang *et al* [33]. In Chang's model, the normal derivative of the potential is zero between neighboring electrodes on the boundary. With this boundary condition, they obtain the analytic solution in agreement with the numerical solution based on the software package Fastflo®. The advantage of using a closed-form solution is that it produces quick and accurate analytical results and no numerical simulation is needed. After plugging in the voltage, I obtained a 2-D electric field in the cross section along the interdigitated array. The streamline of the electric field is plotted in Figure 2-2. A 3-D electric field can be formed by repeating the 2D electric field along the width of the channel since the electrode geometry does not vary along the width of the channel.

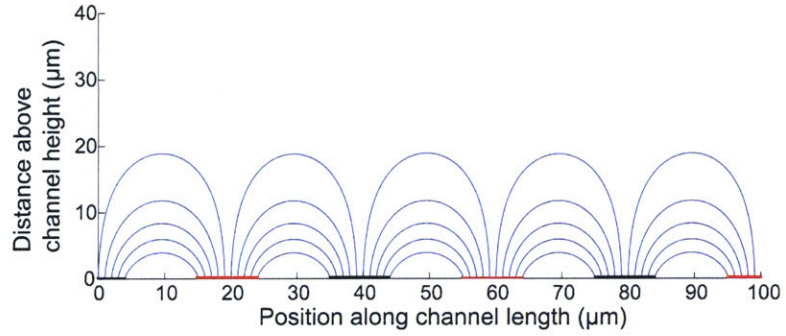

Figure 2-2: Electric field streamlines

Electric field streamlines (plotted in blue) produced by interdigitated electrodes (plotted in black and red) of 10 μm width and spacing.

2.2 Modeling Forces and Particle Motion

The modeling environment calculated the force exerted on the particles to determine the particle motion. It did this by first computing the DEP force, hydrodynamic drag force and gravitational force on the particle everywhere in the space (Figure 2-3), and the virtual wall force that prevented particles from sticking on the wall. Due to the small mass and volume of particles, I can ignore the particle inertia and assume the system is in quasi-steady state. Therefore, the particle responds to the force instantaneously and its movement will follow the direction of the net force. Based on the above assumption, the particle path is the same as the streamline of the force field. I also assumed that all the forces were exerted on the center of the particle and that the particle is much smaller than the fluidic/electric field non-uniformities, so the particle rotation is not accounted for in this case. Moreover, the particles are assumed passive, i.e. they will not influence the fluidic or electric field and there is no interaction between particles.

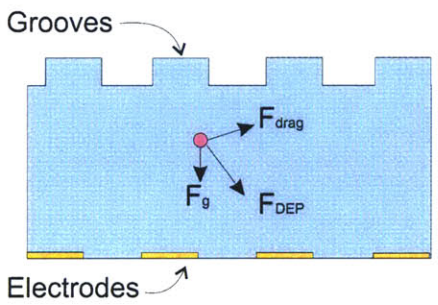

Figure 2-3: Illustration of the forces on a particle

The modeling environment accounted for three forces exerting on the particle: DEP force (F_{DEP}), hydrodynamic drag force (F_{drag}) and gravitational force (F_g).

2.2.1 Particle Properties

To calculate the forces exerted on a particle, the modeling environment has to know the particle information, such as particle radius, density, and dielectric properties. In both simulation and experiment, I use polystyrene beads instead of cells as testing particles because of their more uniform and well-known physical and electrical properties.

To maintain consistent conditions, the particle properties in simulation are based on the beads used in the experiment. More bead information is included in Chapter 4.

2.2.2 DEP Force

The DEP force is the force exerted on the polarizable particle in a spatially varying electric field. Using the obtained electric field, the DEP force can be derived according to the following equation:

$$F_{DEP} = 2\pi\varepsilon_m R^3 \,\mathrm{Re}[CM(\omega)]\nabla E_{rms}^2 \tag{2-3}$$

where E is the complex applied electric field, R is the radius of a spherical particle and $CM(\omega)$ is the complex Clausius-Mosotti (CM) factor. The CM factor is a complex number which provides the strength of the effective polarization of a particle as a function of permittivity. The CM factor for a homogeneous sphere in homogeneous media can be written as follows:

$$CM = \frac{\varepsilon_p - \varepsilon_m - j(\sigma_p - \sigma_m)/\omega}{\varepsilon_p + 2\varepsilon_m - j(\sigma_p + 2\sigma_m)/\omega} \tag{2-4}$$

where ω is the frequency of the electric field, ε is dielectric permittivity, σ is electrical conductivity, and the subscript notations p and m represent particle and media, respectively. The sign of the CM factor dictates the polarity of the dielectrophoretic force. If the CM factor is negative, the particle will undergo nDEP; if the CM factor is positive, the particle will undergo pDEP. The modeling environments take the known analytical electric field, the particle properties, and the calculated CM factor as inputs to compute the DEP forces based on (2-3).

2.2.3 Drag Force

The drag force that a particle experiences in a moving flow is proportional to the particle's velocity:

$$F_C = bv \tag{2-5}$$

where b is the drag coefficient and v is the fluidic velocity. For a sphere particle of radius R in medium of dynamic viscosity η, the drag coefficient is defined as

$$b = 6\pi\eta R \tag{2-6}$$

When extracting the flow velocity solution from COMSOL Multiphysics, I truncate the solution at the edges of the mixer. Because the solution at the edges is not confined by any adjacent mixer/channel, it is not periodic and thus can not be used to cascade a longer mixer. To ensure the fluid flow profile is fully developed and periodic, I extract the solution 2~3 grooves away from the edge.

COMSOL Multiphysics defines and stores the variables in the data structure fem.sol. The *postinterp* command in Matlab allows me to extract the value of the variable and map them onto the x, y and z coordinate system. However, since the geometry of the grooves is arbitrary, while extracting data from COMSOL Multiphysics to Matlab, any attempt to interpolate outside the trimmed surface will result in NaNs in the output. (NaN is the IEEE standard used by Matlab and COMSOL Multiphysics for denoting Not a Number and is the result of expression like 0/0 etc.) I filtered out the numeric value by using the command *isnan* and replace them by zeros. Figure 2-4 shows an example of the velocity vector plane in the cross-section of SHM after all the NaNs are replaced. The processed velocity matrix is then scaled to a desire flow rate and cascaded into any length of a mixer.

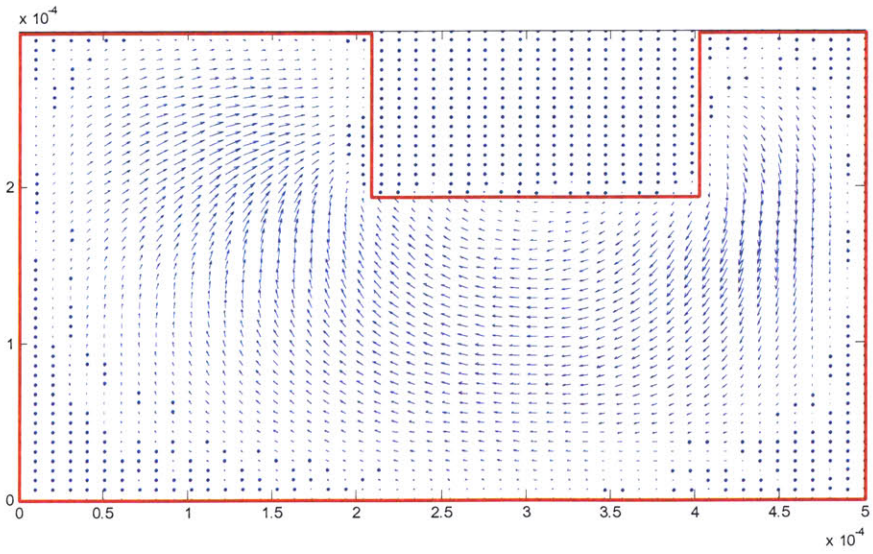

Figure 2-4: Velocity vector plot

Velocity vectors are projected to one of the cross section of SHM. The red profile defines the boundary of the channel. The region outside the trimmed surface is filled with zeros.

2.2.4 Gravitational Forces

The particle in the fluid experiences two gravitational forces. One is the so-called "weight" which is contributed by the particle itself, and the other is the buoyancy force due to the weight of the fluid displaced by the particle. Both of them exert forces on the particle in the z direction, so the magnitude of the combined gravitational forces can be expressed as

$$F_g = \frac{4}{3}\pi R^3(\rho_2 - \rho_1)g \qquad \textbf{(2-7)}$$

where ρ_2 and ρ_1 refer to the densities of the medium and the particle, respectively, and g is the gravitational acceleration constant.

2.2.5 Rigid Substrate and Wall Forces

When my code calculated the motion of the particle, it treated the particle as infinitesimally small and ignored the physical barrier caused by particle volume.

Therefore, the center of the particle is allowed to reach the ceiling, the side walls and the bottom of the channel. Two inappropriate situations will happen when the particle volume is ignored. First, when the center of the particle reaches those surfaces, the particle volume will penetrate the channel boundary, which is physically impossible (Figure 2-5a). Further, those forbidden areas have very small drag forces due to the zero velocity constraint on the wall. Once the particle enters those regions, it is difficult for the particle to get out. For example, Figure 2-5b shows the distribution of the random starting particles after 3 mixing periods. There are a few particles stuck on the ceiling or the side walls due to zero velocity. However, in the experiment, the center of the particle never reaches the wall due to its volume.

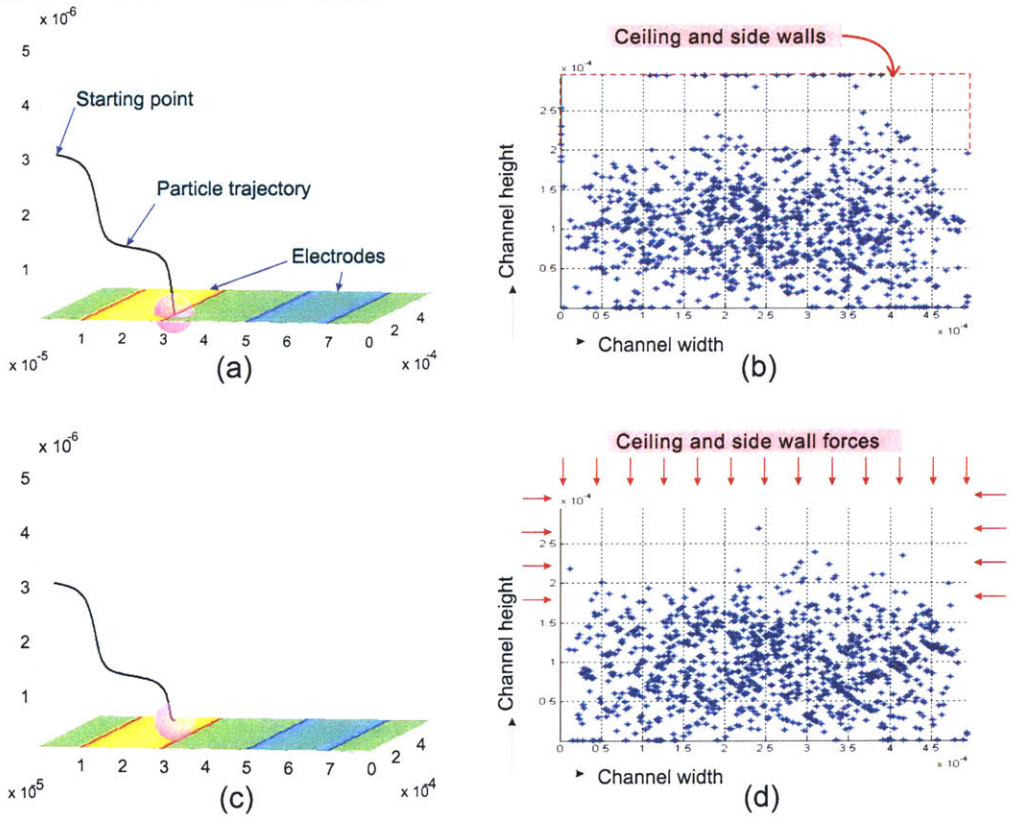

Figure 2-5: Particle motion corresponding to wall force

Before the wall force applied, particles will penetrate the substrate (a) and get stuck on the ceiling and side walls (b) due to the infinitesimally small volume. After the wall force applied, particles can sit appropriately on the substrate (c) and no particles are stuck on the ceiling and walls (d).

To account for the finite size of the particle and keep the particle center away from the boundaries, the modeling environment generated a virtual barrier near the boundaries. The program automatically adjusted the z directed total force on the particle so that it is zero when the particle is sitting on the substrate. Figure 2-5c exhibits the particle sitting properly on the substrate after the force adjustment. However, due to the complicated geometry of the grooves, it is hard to modify the force around the ceiling and the side walls. An alternative way is to assign a wall force to push against the particles and keep them away from the wall. I implement a uniform wall force on the side wall and the ceiling of the grooves (An illustration of the wall force in the cross section is shown in Figure 2-5d). The direction of the added wall force is pointing into channel in order to move the particles away from the wall that they are stuck on. The wall force has to be strong enough to push the particle away from the walls, but not too strong to affect the overall force field. To obtain a proper wall force magnitude, the program used the largest force on the plane next to the walls. Figure 2-5d shows no particles are stuck on the ceiling or side walls after adding in the wall forces.

2.2.6 Particle Motion and Tracking

After constructing the force information everywhere in the channel, the program is then able to compute the trajectory of a particle starting from any point in the channel. The program is capable of starting the particles in an array, specific points or random positions. The tangent of the trajectory is determined by the net force at the particle location. Figure 2-6 shows four computed trajectories starting at the same height from the beginning of the channel. The spiraling trajectories show the effect of mixer, and the blue

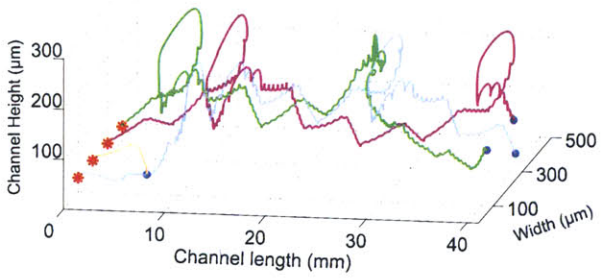

Figure 2-6: Trajectories of particles in SHM

Four particles are started at the beginning of the SHM with the same height (x=0, z=50 μm). One of the particles is trapped by the electrodes; others are swirling through the whole channel.

points represent the final location where the particles end up being. If the trajectory ends on the bottom plane, it means the particle is trapped. On the other hand, if the trajectory finishes at the end of the channel, it means the particle passes the whole channel without being trapped. By counting the percentage of the trapped particles, the program can define the percentage of the particles are trapped with different mixers.

2.3 Fluidic Field Verification

To the best of my understanding, none of the published papers on the chaotic advection mixer have used COMSOL Multiphysics to simulate the flow profiles. Therefore, it is important to verify if the numerical method used for solving the fluidic velocity field gave me a reasonable result. Many numerical or experimental studies of passive micromixers have been presented, and I chose two for comparison with my results: Stroock *et al* [24] demonstrated the SHM mixing results by taking fluorescent confocal images of the vertical cross-section of the channel (Figure 2-7a); and Kang *et al*

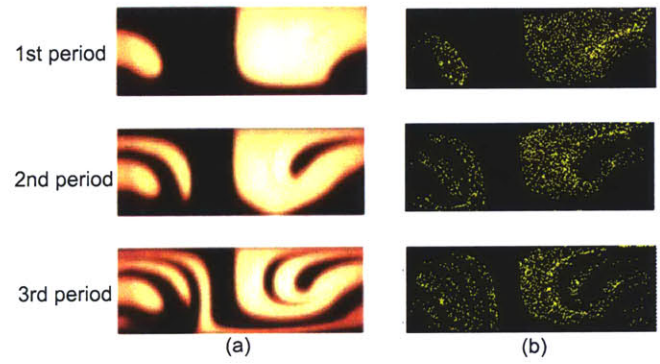

Figure 2-7: Visualization of the SHM mixing pattern (from the 1st to 3rd period)

Vertical cross section images show the rotation of the colored stream and clear stream injected along either side of the channel. (a) Fluorescent confocal micrographs reproduced from [24] (b) Particle tracking image obtained from numerical simulation. The geometry parameters of (b) are similar to those of (a).

[25] visualized the SGM mixing pattern by illustrating the Poincaré sections generated by their numerical scheme (Figure 2-8a). In these two papers, they both injected two streams on each side of the channel, and observed the mixing pattern either experimentally or numerically. The results in both papers are in agreement with each other, so I chose them as references for my mixer simulation.

I used my simulation method to mimic their experiment/simulation. Since the verification is only for fluidic fields, the electric field is not applied in those cases. The Poincaré sections I obtained are shown in Figure 2-7b and Figure 2-8b. The mixing patterns acquired by my simulation are almost identical to theirs. This implies that by using my simulation scheme, I should be able to obtain a reliable flow field and predict the overall mixing trend.

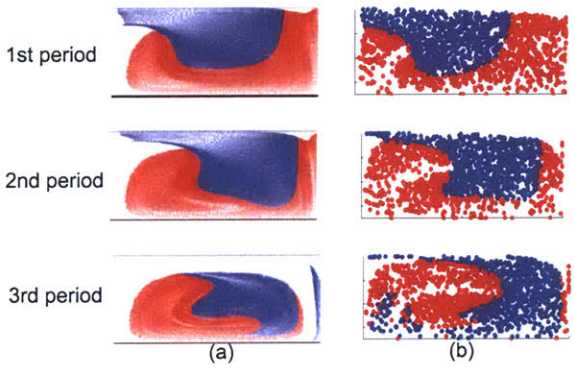

Figure 2-8: Visualization of the SGM mixing pattern (from the 1st to 3rd period)

Vertical cross section images show the rotation of a red stream and a blue stream injected along either side of the channel. (a) Colored particle tracking results reproduced from [25]. (b) Particle tracking images obtained from numerical simulation. The geometry parameters of (b) are similar to those of (a).

2.4 Design

2.4.1 Electrode Width and Spacing

DEP forces generated by interdigitated electrodes exhibit a tradeoff between the DEP strength and the decay rate of the DEP strength away from the electrode. This tradeoff is controlled by the width and spacing of the interdigitated electrodes. Wider electrodes with larger spacing have weaker DEP force but a slower decay rate while narrower electrodes with smaller spacing have stronger local electric field strength but a faster decay rate. DEP force with a slower decay rate can extend the force farther away from the electrode and reach the particles in higher position. On the other hand, stronger but localized DEP forces can hold the particle against a larger flow rate.

Figure 2-9 shows the contour plot of the logarithm of the DEP strength generated by different width and spacing electrodes. The 10 μm width and spacing electrode exhibit the fastest decay rate of the DEP; the 20 μm exhibits an intermediate decay rate, and the 50 μm pitch exhibits the slowest decay rate. However, by reading the color bar in each picture, one can tell that the largest DEP force happens in 10 μm case (>log10^{-7}), and the second and the third largest happen in 20 μm and 50 μm respectively.

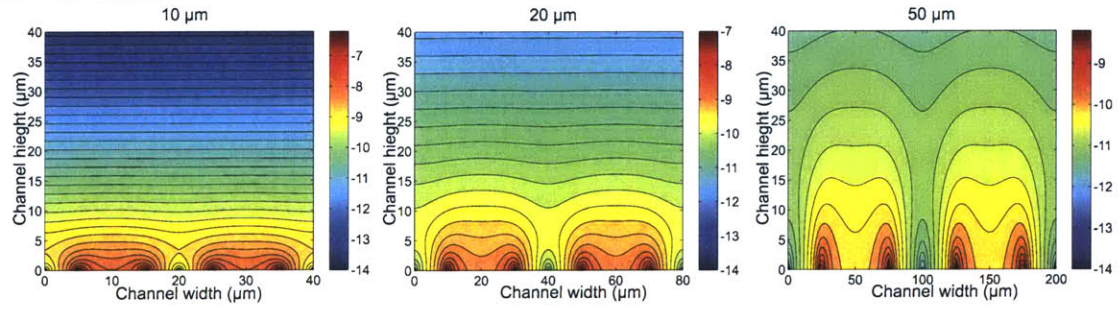

Figure 2-9: Contour plot of logarithmic DEP force

The DEP force generated by different width and spacing electrodes have different strengths and decay rates. The DEP force has the highest local maximum (>log10^{-7}) in the 10 μm case. However, the DEP force decays slowest away from the 50 μm case. The 20 μm case performs an intermediate local maximum strength and decay rate.

For the concentrator with a mixer, the function of the electrodes is more likely to hold the particles rather than reach the particles. Since the mixer will circulate the flow, it sends the particle to the electrodes more efficiently; therefore, narrow electrodes with a stronger DEP force are preferred in this case. Furthermore, when characterizing the trapping efficiency with mixer, I care more about the performance difference between each mixer than the overall trapping efficiency, so I chose 20 μm electrode widths which have decent DEP strength and are easy to fabricate.

2.4.2 Mixer Geometry

I start the design with two existing mixer patterns: the slanted groove mixer (SGM) and the staggered herringbone mixer (SHM). The mixing performance is highly associated with the geometry of the mixer pattern. Figure 2-10a and b illustrate the trajectories of two representative particles in those two mixers. In the SGM, the slanted grooves guide the flow to move in a circle. Particles in SGM have their own orbits with respect to the centerline (Figure 2-10a). It is obvious that the inner particle can hardly penetrate the outer orbits and get close to the bottom where the interdigitated electrodes are. However, the outer particles have sufficient chance to enter the DEP effective region and get trapped. In SHM the situation is different. Its asymmetric herringbone grooves create two circles of flow, but the circles are different in size. In addition, for every half circle, the centers of the circles exchange their positions due to the change in the position of the asymmetric herringbone tip. Therefore, the flows will reconstruct every half circle constantly, and the direction of rotation alters at the same time as shown in Figure 2-10b. These characteristics make SHM a chaotic mixer which has better mixing efficiency than SGM.

Inspired by the mixing characteristics of SGM and SHM, I created another mixer pattern: symmetric herringbone. In order to distinguish it from SHM, I named it the herringbone mixer (HM). In HM, the flow is split by the herringbone grooves into two streams to create two rotation circles in equal size (Figure 2-10c). With the symmetric geometry, the HM is not like the SHM, which is a chaotic mixer. It exhibits a regular mixing pattern like the SGM, but lifts and brings the particles to a different position. The benefit of having the HM is that it not only provides a comparison between staggered

herringbone and symmetric herringbone but also offers a regular mixing pattern that can be combined with the SGM. Using the HM after the SGM (SHM+HM) can help the particles in the middle of the channel move toward the bottom and hence increase the number of trapped particles.

Most of the published papers used the mixer dimensions defined in [24, 26] that produced optimal mixing. I used the same geometry parameters, but to achieve a higher flow rate I modified the average channel height to 250 μm and channel width to 500 μm. Changing the channel height and width might affect the optimal mixing efficiency since the mixing performance is very sensitive to the geometry. However, so long as the mixer still exhibits its characteristics, the modification is acceptable. The dimensions are illustrated in Figure 2-11 and summarized in Table 1.

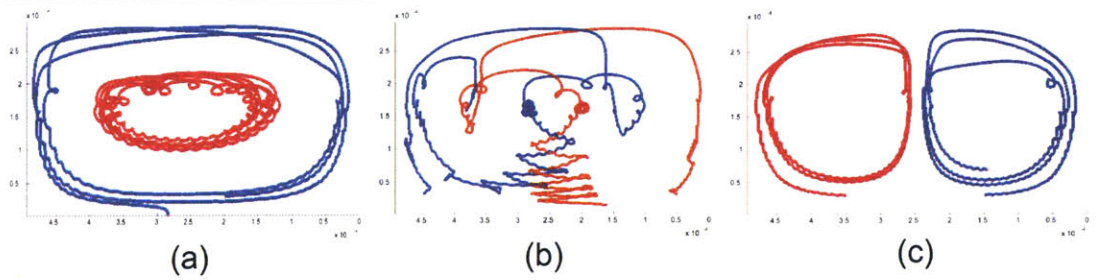

Figure 2-10: Trajectory plots

Two representative particle trajectories are plotted to illustrate the mixing characteristic of (a) SGM, (b) SHM, and (c) HM.

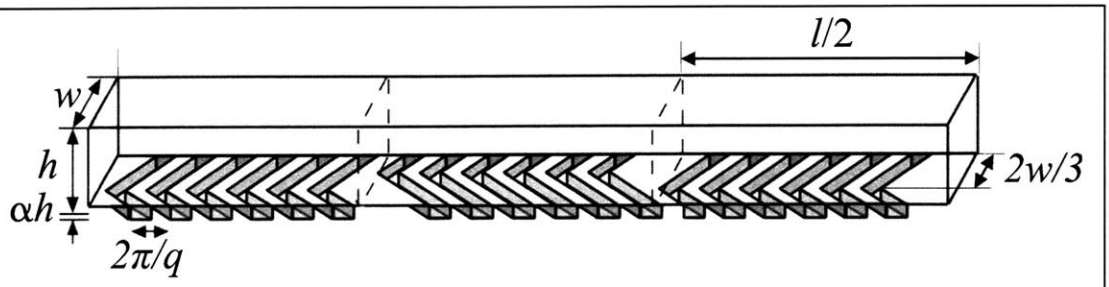

Figure 2-11: Mixer dimension

The illustration shows the definition of the dimension parameters of SHM. Note that h defines the *average* channel height (channel depth plus half the mixer grooves), and αh defines half the mixer groove depth. The values assign to the parameters are listed in (Table 1). The image is adapted from [24].

Table 1:Channel dimensions based on mixer publications.

Name	Description	Value	Note
h	Average channel depth	250 μm	Chosen to increase flow rate
w	Channel width	500 μm	Chosen to increase flow rate
α	Half groove depth	0.2	-
q	Principal wavevector of the groove	400 μm	-
l	length of one mixing cycle	4.8 mm	l/q=12
r	Groove asymmetry	2/3	Applicable only to SHM

Chapter 3: Microfabrication and Packaging

The device has two main components: interdigitated electrodes and a micromixer. Both of them have micron-scale features, so microfabrication is required. The microfabrication of the device was processed in a cleanroom with common MEMS techniques. After the main components were made, they were assembled and package with other assisting components to connect the devices to the macro scale world. In this chapter, I describe the design of masks for photolithography and the fabrication process of the electrodes and micromixers. The device package is included at the end of this chapter as well.

3.1 Masks

Two sets of masks were required for the fabrication of both the interdigitated electrodes and the SU-8 structure. Specifically, the electrode photolithography needed one mask and the SU-8 structure photolithography needed two masks since it was a two-layer process. All of the three masks were 7" chrome upright reading masks (Fineline Imaging, Colorado Springs, CO).

3.1.1 Electrode Mask

The mask for the electrode photolithography is bright-field because the following liftoff process uses image-reversal photoresist. Figure 3-1 shows the pattern of the mask drawn by AutoCAD. There are 12 dies in the mask arranged in the same orientation and surrounded by border lines for the later step of dicing. The 12 dies included three different sizes of electrodes: 10, 20, and 50 μm width and spacing which were simulated in the previous chapter. All the electrodes were divided into four pairs. This is not only to increase the device yield but also to enable the application of different voltages on different sections of the electrodes. Figure 3-1a is a magnification of one pair of interdigitated electrodes. Figure 3-1b is the close-up of the marks used for fluidic access holes. These markers indicated the location of the inlet and the outlet of the fluidic channel and they helped with the alignment for drilling the holes. The text on the upper

and lower left of each die provides the information specifying the mask version and the electrode dimension, respectively.

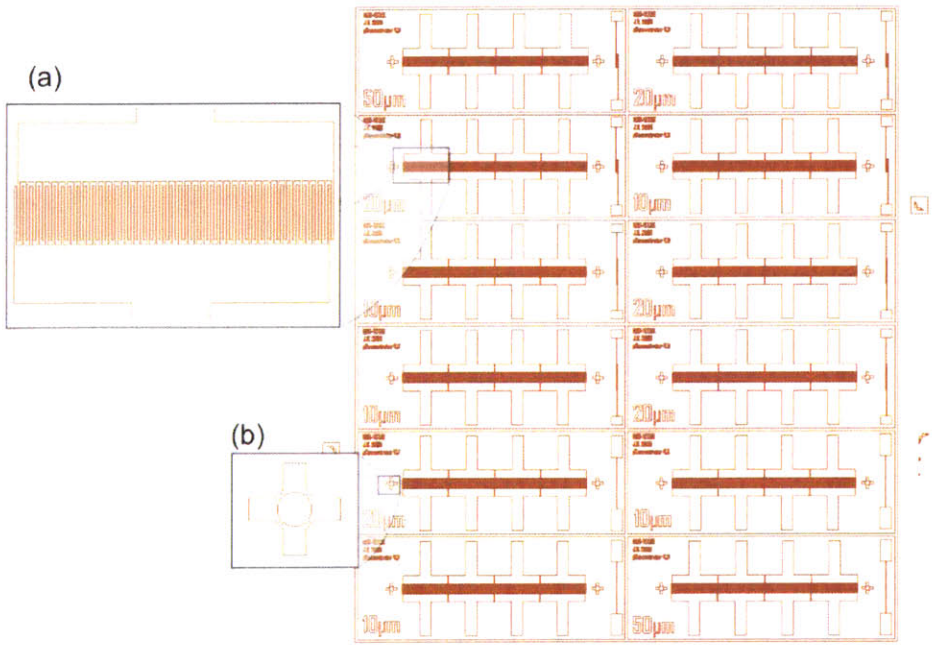

Figure 3-1: Electrode mask

The background shows the overview of the electrode mask. (a) A magnification of one set of 20 μm electrodes. (b) A magnification of a fluidic access hole marker.

3.1.2 SU-8 Mask

The SU-8 structure for molding the PDMS channel consisted of two layers. The bottom layer defined the fluidic channel and the top layer defined the pattern for the mixer (shown in red and blue in Figure 3-2, respectively). Each of the layers needed its own mask for photolithography. Both masks are dark-field because SU-8 is a negative photoresist.

The first mask (shown in pink in Figure 3-2) patterned 18 channels which all had the same dimension. Each die is surrounded by border lines which not only define the boundary of each die, but also help in cutting the molded PDMS. At the ends of every channel, a round shaped reservoir was used to connect the channel to the fluidic access

hole on the electrode die. Text describing the device version and mixer label were also included in the first mask.

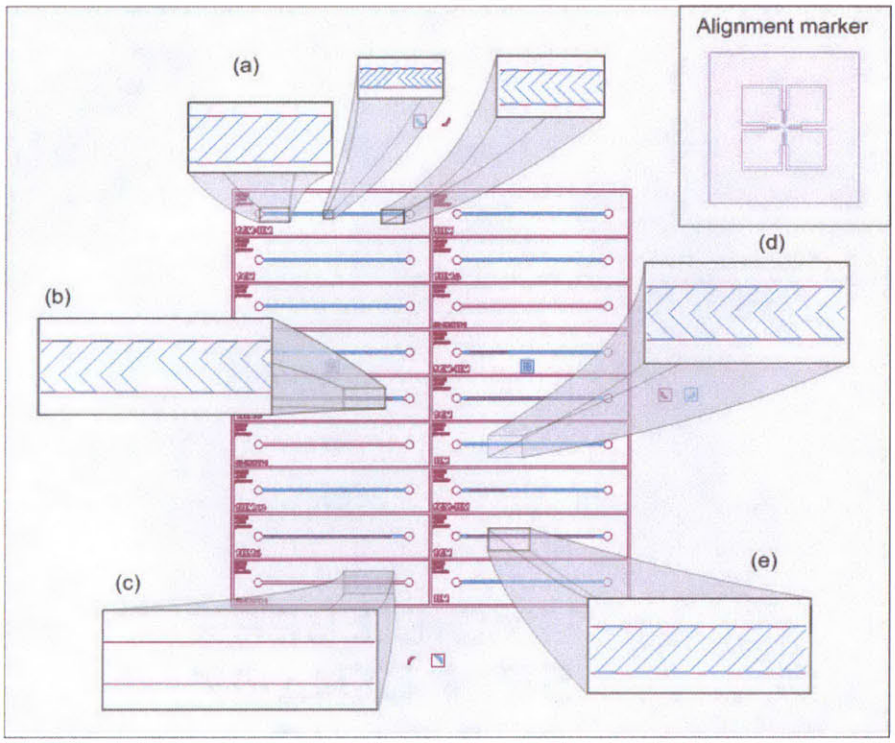

Figure 3-2: Micromixer mask

The background shows the overview of the micromixer mask. The subfigures show the magnification of (a)SGM+HM, (b)SHM, (c)Smooth channel, (d)HM, and (e)SGM. The upright insert is a close-up of a cross-hair alignment marker.

The second mask (shown in blue in Figure 3-2) patterned the mixer grooves on the top of the channel. Three types of mixer patterns, SHM, HM and SGM (Figure 3-2b, d, e, respectively) which I characterized in the simulation are included in the mask. A combination mixer SGM+HM (Figure 3-2a) is the design composed of SGM and HM. Figure 3-2c shows a smooth channel which has no mixer pattern on the second mask. All the grooves started right after the inlet reservoir and ended right before the outlet reservoir to ensure the liquid was being mixed all the way through the channel.

The alignment of the two masks is done via two cross-hair alignment markers in the middle of the masks (Figure 3-2 insert). The window around the cross-hair alignment

marker on the mixer mask provides the visual access to the counter part cross-hair marker on the channel mask.

3.2 Microfabrication

The electrode chip and the SU-8 mixer structure were fabricated in MIT's Technology Research Laboratory class 100 cleanroom. The fabrication process was modified based on [9]. The complete outline of the fabrication process is included in Appendix, and the details will be described in the following sections.

3.2.1 Au Electrode

I chose 6" Pyrex wafers (Bullen Ultrasonics, Eaton, OH) to be the substrate for the electrodes because of Pyrex's electrical isolation properties and for optical access. Although Pyrex has relatively lower thermal conductivity compared to silicon, it is still a proper material if the power dissipation is insignificant. According to the device design, low conductivity media will be used for generation of positive DEP, so little power dissipation through the device is expected. Therefore, Pyrex is an appropriate material as substrate for electrodes.

I chose Au to be the material for the electrodes because of its bio-compatibility. A liftoff process is used to pattern the electrodes. The benefit of using a liftoff process rather than chemical etching is that there is no worry of selecting a proper etchant and finding the proper time/speed for etching. An additional benefit is that I can pattern multilayer films (Au + Ti adhesion layer) in one step.

The preparation for the liftoff process includes a wafer clean, dehydration and adhesion promotion. First, I cleaned the Pyrex wafer with a standard Piranha (1:3 H_2O_2:H_2SO_4) cleaning process to remove organic contamination. Second I rinsed the Pyrex wafer with DI water and dehydrated it in the oven. Third, before depositing photoresist on the wafer, I coated it with Hexamethyldisilizane (HMDS) to provide a better adhesion between photoresist and Pyrex wafer.

Figure 3-3 shows the main steps of the liftoff process. First, I spun a layer of image-reversal photoresist AZ5214 (Figure 3-3a). AZ5214 is a positive photoresist whose polarity can be reversed by a flood exposure. To pattern the photoresist, I prebaked the photoresist, exposed it with through the mask with features I wished to keep, and then postbaked it. Then I flood exposed the entire wafer to reverse the polarity of the photoresist and developed it in AZ422 developer. Figure 3-3b shows the developed pattern. After development, I rinsed the wafer with DI water and spin-dried it.

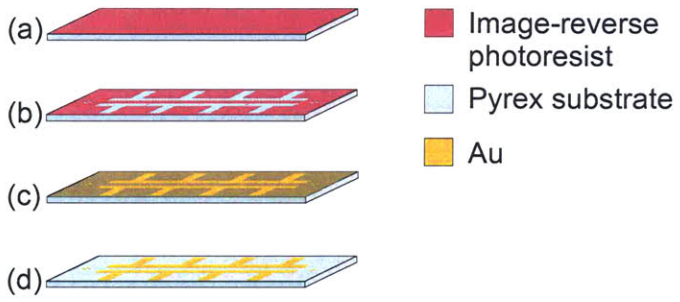

Figure 3-3: Gold liftoff process

Microfabrication process for the gold interdigitated electrodes. Four main process steps: (a) photoresist coating, (b) photoresist development, (c) Au deposition, and (d) Au liftoff.

The next step is deposition of gold. To promote the adhesion between gold and Pyrex substrate, I deposited a 100 Å thick titanium layer before the deposition of the 2000 Å thick gold layer. Both the titanium and gold are evaporated by e-beam and deposited on the Pyrex wafer (Figure 3-3c). After deposition, I soaked the whole wafer in acetone to dissolve the photoresist. While the photoresist was dissolving, the unpatterned gold peeled off from the Pyrex substrate (Figure 3-3d). I observed that for tighter electrodes, the gold was harder to remove and sometimes when it came off, it tore the patterned gold off as well. To help the unpatterned gold come off cleanly, I soak the wafer in an ultrasonic water bath after acetone soaking. The ultrasonic vibration of the water helped the residual gold peel off. When ultrasonically bathing the wafer, I kept the side with the gold facing down so that any waste would not gather on the wafer.

The last step is to dice the wafer. Before dicing, I spun a thin layer of photoresist to prevent the electrodes from contamination and damage during dicing. This layer of photoresist also protected the electrodes when the fluidic access holes were dilled during the later packaging. A fully-processed die is shown in Figure 3-4a and the magnification of the 50μm width and spacing electrode under microscope is shown in Figure 3-4b.

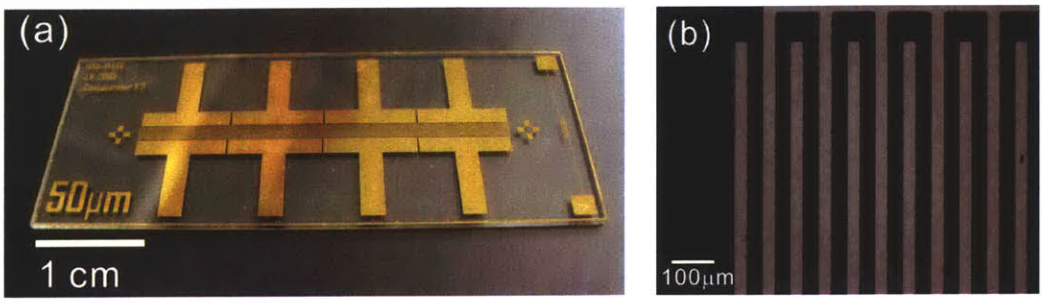

Figure 3-4: Gold interdigitated electrodes

(a) Fully fabricated electrode die. (b) A magnification of electrodes taken via microscope.

3.2.2 SU-8 Mold and PDMS Micromixer

I used SU-8 2050 to make the structure for molding the PDMS channel. SU-8 is a photodefindable, epoxy-based negative resist. It is widely used in patterning microfluidic channels because it is easy to fabricate high-aspect-ratio structures and one SU-8 mold is durable for molding several PDMS channel duplicates.

The micromixer has a 200-μm-high channel and a 100-μm-high mixer pattern. To obtain a uniform thickness of SU-8, I only spun 100 μm per coating step. In other words, the channel comprises two layers of 100-μm-thick SU-8 and the mixer pattern comprises one layer. I estimated the spin speed, baking time and exposure time according to the datasheet on the MicroChem website.

I started the process with a blank silicon wafer (WaferNet, San Jose, CA.) I first dehydrated (200 °C, 30mins) the wafer to promote the adhesion of SU-8. Then I spun the first 100-μm layer of SU-8 with 2 speed cycles (spread cycle: 500 rpm, 20 secs; spin cycle: 1680 rpm, 30 secs) and prebaked the layer (65 °C, 5 mins, 95 °C, 10 mins). I prebaked this layer with a shorter time compared to the suggested time on the MicroChem website because there was another prebake step (65 °C, 5 mins, 95 °C, 30 mins) after the second 100-μm layer. After spinning and prebaking two 100-μm layers (Figure 3-5a), I patterned the channel structure (36 sec, 10 mW/cm2/sec, 365-405 nm) (Figure 3-5b) with the first mask mentioned in SU-8 mask section. After post-bake (65°C, 1 min, 95°C, 9 mins), without developing the channel structure, I spun the third 100-μm layer (Figure 3-5c). I prebaked (65 °C, 5 mins, 95 °C, 60 mins), patterned the grooves (23 sec, 10mW/cm2/sec, 365-405 nm) and post-baked it (9 mins, 95 °C) (Figure 3-5d). To develop the structure, I soaked the whole wafer in PM Acetate to dissolve the unexposed part of the SU-8 and gently wiggled the container to help the SU-8 dissolve. To check if the development was done, I spread isoproponal alcohol on the wafer. The

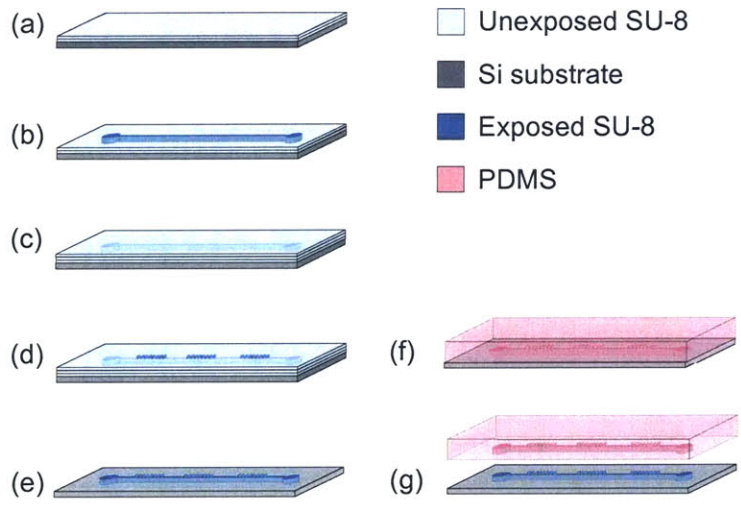

Figure 3-5: SU-8 structure and PDMS micromixer fabrication process

The microfabrication process of SU-8 structure and PDMS micromixer. Seven main process steps: (a) coating 1st layer of SU-8, (b) patterning the channel, (c) coating 2nd layer of SU-8, (d) patterning the grooves, (e) development, (f) casting PDMS, and (g) peeling off the molded PDMS.

undeveloped SU-8 will turn milky when in contact with isoproponal alcohol. After fully developing the SU-8, I spread PM Acetate to wash out the waste and air dried the wafer. I then placed the wafer in a vacuum jar with several drops of HDMS for 1 hr to silanize the SU-8 surface. Silanization is for satisfying the dangling bonds on the SU-8 surface with HDMS molecules. It prevents PDMS from bonding to SU-8.

During the SU-8 process, I found that the uniformity of thick SU-8 was poor and a lump of SU-8 occurred on the edge of the wafer. The lump of SU-8 was soft even after prebake. This bump made the wafer stick to the mask during the photolithography process. To improve the uniformity, I used the two cycles of spin recommended by MicroChem. The first cycle is a spread cycle which allows the SU-8 to cover the entire surface and the second cycle is spin cycle which spins the SU-8 to the final thickness. The recommend spread cycle is 5~10 secs, but I used 20 secs for my case to achieve better results. In addition, elongating the prebake time can harden the SU-8, so it is more difficult for the SU-8 to stick to the mask. A front-side protection tape can be used to cover the sticky part of the SU-8 if the sticking problem is still major.

I cast PDMS into the SU-8 mold to make the micromixer (Figure 3-5f). I poured about a 5-mm thick layer of PDMS (10:1 base:curing agent by weight) on the wafer and baked it until it cured (65°C, 3 hrs). After curing the PDMS, I gently peeled the PDMS off from the wafer (Figure 3-5g) and cut the PDMS into individual devices. One piece of PDMS containing a micromixer is shown in Figure 3-6a. Figure 3-6b is a magnification of a SGM pattern.

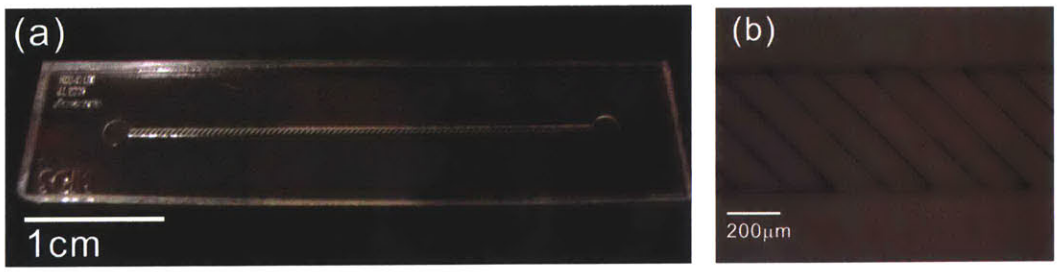

Figure 3-6: PDMS micromixer

(a) A piece of PDMS micromixer. (b) A magnification of SGM groove pattern under microscope

3.3 Packaging

The package not only protected the fragile fabricated die, but also interfaced between the micro-scale components and the macro outside world. I employed the packaging scheme developed in [34]. The packaging integrated the fluidic and electrical system as well. After packaging, a fully functional device is then completed. In this chapter, I describe the design of the main package component: the printed circuit board and the assembly of all the components.

3.3.1 Printed Circuit Board

The printed circuit board (PCB) (ExpressPCB, Santa Barbra, CA) is the main component for interfacing the die to the outside world. The PCB provided both electrical and fluidic access. Figure 3-7 (Left) indicates the configuration of the PCB. Red lines represent the traces on the top of the PCB and green lines represent the ones on the bottom. The circles indicate the punched holes where the headers, wires, and fluidic tubing are placed. There are four sizes of punched holes on the PCB: 0.04", 0.046", 0.061", and 0.125". The 0.04" and 0.046" holes have electric usage and are connected by traces. The 0.046" holes are for the wire connecting the die and the PCB circuit. The 0.04" holes are where to place headers. There are two kinds of header configurations. The stand-alone headers such as V1, V2 and GND are used to connect the device to a

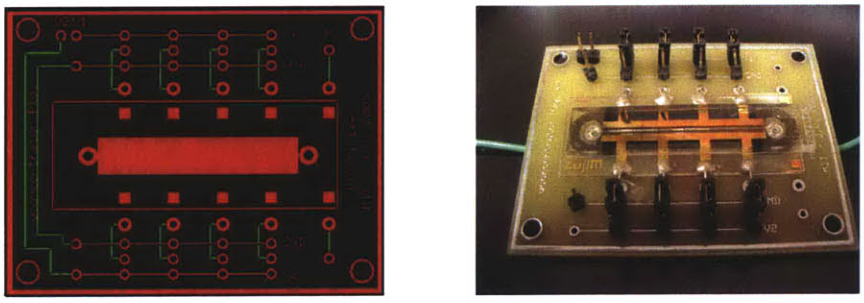

Figure 3-7: PCB layout and packaged device

The left shows a PCB design for packaging the device. The round features are through holes connected by traces on the top or the bottom of the PCB. The right shows the finished package consisting of headers, jumpers, NanoPort, tubing and die.

function generator. The headers lining vertically in a set of three are for the connection between electrodes and a voltage or ground. In addition, the middle header of the three is connected to the electrode by the green traces. The other two headers are connected to a voltage or ground by the red traces. By placing the jumper on the headers, the middle one can be shorted to either of the other two and hence the voltage applied on the electrodes is determined. The 0.061" holes are the fluidic accesses that align with the holes on the die and connect to the fluidic tubing. The 0.125" holes are for fixing the PCB to the foundation with screws.

The red traces which were not connected to any holes were used for alignment. They indicated the border of the die and the electrode contacts. In particular, the red block in the middle of the PCB is the metal plating for blocking the autofluorescence of the PCB. It is important because the emitted fluorescence of PCB will overwhelm that of the testing beads. By placing the metal sheet under the fluidic channel, the background fluorescence can be eliminated.

3.3.2 Assembly

I started the assembly with Pyrex die preparation. I drilled the fluidic access holes where the markers are illustrated in Figure 3-1 with a 0.75-mm-diameter diamond drill bit (C. R. Laurence Co., Inc., Los Angeles, CA). After the holes were drilled, I rinsed the die with acetone, methanol and isopropanol to dissolve the photoresist applied on the Pyrex for protecting the electrodes from drilling damage. I air dried the die after rinsing it.

I then attached the die onto the PCB. I placed two NanoPort adhesive rings (Upchurch, Oak Harbor, WA) around the fluidic access holes on the PCB. The NanoPort adhesive ring not only adhered the die to the PCB, but also sealed the connection to form a fluidic access. The NanoPort required compression and baking to fully adhere to the surface, so I clamped the device with binder clips and baked it in the oven at 65°C for a few hours. While clamping the device, I placed a piece of PDMS and a glass slide on the die to prevent it from directly contacting the binder clips and to provide an even compression.

After the NanoPort fully set, I made electrical connections between the die and PCB. I used conductive Epoxy (ITW Chemtronics, Kennesaw, GA) to glue one end of the wire to the electrode contact on the die and soldered the other end to the PCB. I also soldered the headers introduced in the previous section to the PCB. Then, I inserted 1/16"-outer-diameter PEEK tubing (Upchurch) into the fluidic access holes from the back of the PCB. I sealed the tubing with High Performance Epoxy (Loctite Inc., Pocky Hill, CT). I then baked the device at 65°C for 1~2 hours to cure the epoxy.

I did not bond the PDMS micromixer to the Pyrex using plasma bonding. Instead, I clamped the device with binder clips to provide a normal pressure on the PDMS micromixer to seal the channel. Since the PDMS is not permanently bonded to the Pyrex die, it is easy to replace the micromixer on the device. A packaged device is shown in Figure 3-7 (Right).

Chapter 4: Device Testing

To evaluate the fabricated device and verify the results predicted by the simulations, I designed a test setup and performed experiments. In this chapter, I describe the materials and tools used in the test setup and the measurement method developed for the experiments.

4.1 Materials and Tools

4.1.1 Test Particles

Although the ultimate objective of the device is to concentrate microorganisms such as *B. subtilis endospores* and *Escherichia coli*, it is challenging to evaluate the device performance with microorganisms since they have unknown and dynamic properties. Since the essential goal of these experiments and of my thesis is to verify the simulation and characterize the mixer performance, using artificial particles that have well-defined properties and easier modeling parameters is more practical.

I chose two kinds of fluorescent carboxyl-modified polystyrene beads. The first particles are 1-μm-diameter fluorescent pink Carboxyl magnetic microspheres (Spherotech, Libertyville, IL) and the second particles are 1.75-μm-diameter fluoresbrite blue Carboxylate microspheres (Polysciences, Warrington, PA). Both types of beads are at the size of interest (~1 μm). There are also many benefits to using fluorescent beads. Under fluorescence imaging, the fluorescent beads will appear much brighter than the background, greatly improving the contrast between the fluorescent beads and the background. This is a necessary requirement for good image acquisition. The fluorescent beads also exhibit negligible photobleaching, which is good for maintaining the image intensity and quality. The excitation and emission wavelengths (nm) are 560, 590 for pink beads and 360, 407 for blue beads, respectively.

The material of the beads is polystyrene, which has lower conductivity than water, so the beads will exhibit nDEP under any frequency. However, the carboxyl surface modification forms a negatively-charged layer on the surface of the bead. Since the surface to volume ratio is relatively large for the small beads, the surface charge will

dominate the bulk dielectrophoretic properties and therefore the surface-modified beads exhibit higher conductivity than the water with conductivity from 5.5e-6 to 1e-4 S/m and experience positive DEP in the water. Both of the beads were characterized for their dielectrophoretic properties in [9, 35]. The references suggest that the optimal operating frequency for both beads is about 100 kHz

4.1.2 Test Setup

The test system consisted of the packaged device, the fluidics, the driving electronics and the optics. Figure 4-1 illustrates the integration of the system. For the fluidics, I used a syringe pump (KD Scientific 200, Holliston, MA) to drive two plastic syringes loaded with water and Alconox (Alconox, White Plains, NY). The syringe pump controlled the flow rate of liquid through the device. Between the syringes and the device, there are two valves to manage the input media and sample. Valve 1 is a 4-port valve which was switched between water and Alconox. Valve 2 is a 6-port valve which has two operating modes. Mode 1 is for loading a fixed volume of sample; mode 2 is for injecting the sample into the device. All the fluidic components are connected up by 1/16"-outer-diameter PEEK tubing.

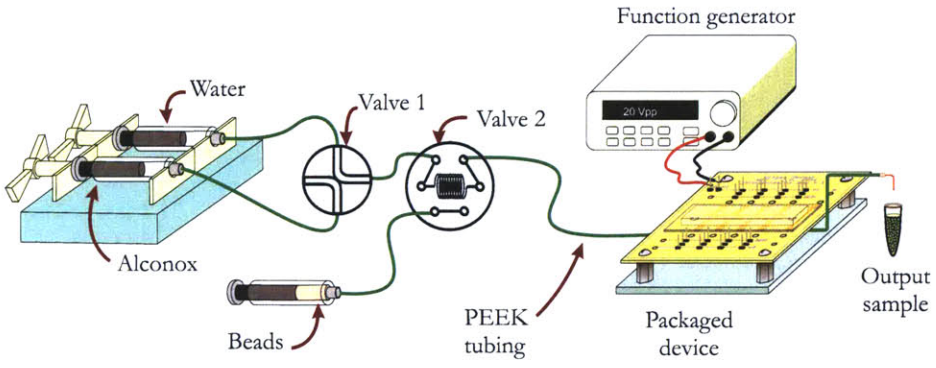

Figure 4-1: Experimental setup

A function generator (33220A, Agilent, Palo Alto, CA) was connected to the device to provide an AC power supply for generating DEP force. The function generator can produce sinusoidal waves up to 20 volts peak-to-peak over an available frequency range of 1~80 MHz. An oscilloscope (Tektronix, Richardson, TX) was hooked up with the device to monitor the actual voltage across the channel.

A Zeiss Axio Imager reflected-light microscope (Zeiss, Thornwood, NY) is the tool used for optically monitoring and observing the experiment results. The microscope uses a white light source generated by a halogen light bulb and fluorescent light source generated by a Xe light bulb. The filters 31000 and 31002 (Chroma, Long Beach, CA) on the microscope have the corresponding bandwidth for the fluorescent testing beads described in section 4.1.1. The optical images were taken via Sensicam QE cooled CCD digital camera (The Cooke Corporation, Romulus, MI). To take images along the entire channel, I manipulated the microscope stage with a Matlab program to control the step size of the scan.

4.2 Measurement Method

To quantify the number of the trapped beads, two feasible measurement methods are considered. The first method involves developing a visual counting algorithm to measure the number of beads in the channel; the second method involves is using spectrophotometer to measure the output sample concentration.

For the second method, completely releasing particles from the electrodes and collecting them into an output sample is a major challenge when the particles are small. Since the surface-to-volume ratio of small beads is high, the surface adhesion force overwhelms the fluidic drag force. Applying a surface coating on the substrate containing electrodes can reduce adhesion to the surface [9], but the coating degrades after several runs of the experiment in a single device. The advantage of visual counting is that it counts the trapped beads inside the device and does not require the release of particles from the DEP electrodes. Moreover, by taking an image of the trapped beads inside the device, the image counting method can provide not only the concentration of trapped beads, but also the trapped bead distribution along the channel, which will give more detailed information necessary for characterizing mixers. Thus I chose to develop a visual counting algorithm, described in the next section.

4.2.1 Image Processing Algorithm

To visually count the beads, I need to develop a reliable image processing algorithm. One straightforward algorithm involves measuring the overall fluorescent intensity of the image and dividing it by the intensity of one bead. While this method works for an image with perfect contrast between beads and the surrounding medium, the intensity measurement is very sensitive to the image quality, which in reality is affected by background noise, exposure time and focusing accuracy. These factors make the image quality vary from image to image, making it hard to find a reliable calibration curve. To demonstrate the actual behavior of an intensity measurement, I performed a preliminary experiment with an intensity-based measurement. I first flowed a bead sample whose concentration has been measured on a hemacytometer (VWR, Westchester, PA) into the device. I then stopped the flow, took images of the beads in the channel and measured the intensity of the image by Matlab. Based on the measurement results, I produced a set of calibration curves of the measured intensity versus the sample concentration (Figure 4-2). It is clear that the intensity is not linearly proportional to the

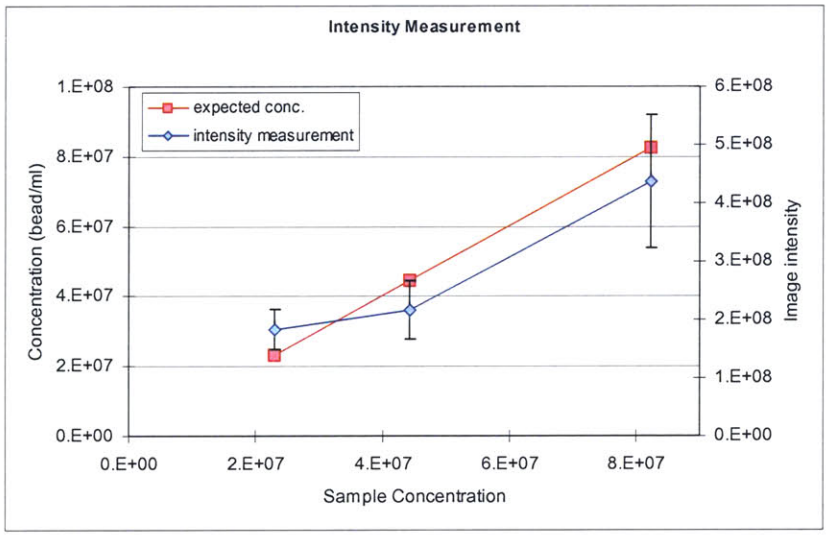

Figure 4-2: Intensity to concentration calibration

A plot of measured intensity versus known concentration is given. While the intensity matched reasonably well to expected intensity, the error associate the measurement is too large.

sample concentration and the standard deviation of the data point is too large to be a good reference. It is also impossible to do any image processing on the raw image without affecting the intensity profiles of the image. These two properties make direct intensity-based concentration measurement difficult.

The other way to quantify the bead concentration is to convert the intensity image into a binary image and count the number of objects in the binary image. This algorithm does not directly rely on the intensity, which fluctuates due to many external factors. The counting is instead based on the morphology of the beads, where an object is defined by the connection of the non-zero values in a binary image. Many other image processing tools use a similar algorithm to measure the properties of objects in the picture. Matlab's image processing toolbox also provides functions for binary counting algorithms. Therefore, I decided to use a binary algorithm, which is described in detail in the following paragraphs.

I wrote a program utilizing Matlab image processing functions which calculate statistics about objects in the image. The program has three main functions: image preprocessing, converting intensity images to binary images and counting objects. The first function is written to optimize the image quality for achieving better results. Optimization can be achieved by performing general image processing. The program first defines and subtracts the background from the raw image (Figure 4-3a) with command *imopen* and *imsubtract.* It second adjusts the contrast by the following code:

```
Imax = max(max(I));  % maximum in I (I is the intensity matrix)
I = I/Imax;          % normalized I by Imax
I = I.*I;            % increase contrast
I = Imax*I;          % restore I
```

These types of adjustments further enhance the contrast ratio between the beads and the background. The second function's purpose is to convert the intensity image into a binary image. One straight forward algorithm for converting the image is to set an absolute threshold, so that the intensity higher than the threshold is labeled as 1 and otherwise as 0. The program can automatically compute an appropriate threshold by using the command *graythresh.* However, when two particles are very close to each other, the intensity profiles in their vicinity are superimposed, so the vicinity intensity

may be higher than the threshold and that area will be labeled as 1 in binary image as well (Figure 4-3a, b, white arrow). The area between the two closely spaced objects will connect them together in the binary image, making them indistinguishable to an adjacent intensity based counting algorithm. To better distinguish between two nearby particles, I used another conversion algorithm which first uses morphological grayscale reconstruction [36] to find the extended region of the local maximum and then returns a binary image which marks the extended region. The method is suitable for distinguishing between two closely spaced peaks, even when the vicinity is brighter than the background. However, this conversion process will cause some of the small peaks disappear after the reconstruction, allowing this method to miss some dim particles (Figure 4-3a, c, yellow arrow). To maintain the successful conversion qualities and to compensate for the errors inherent in these two algorithms, I applied the first algorithm to individually dim particles and the second algorithm to clumped bright particles. I counted the number of beads in each binary image separately and then superimposed two images together (Figure 4-4d) to eliminate the overlapped objects which are counted twice by both algorithms.

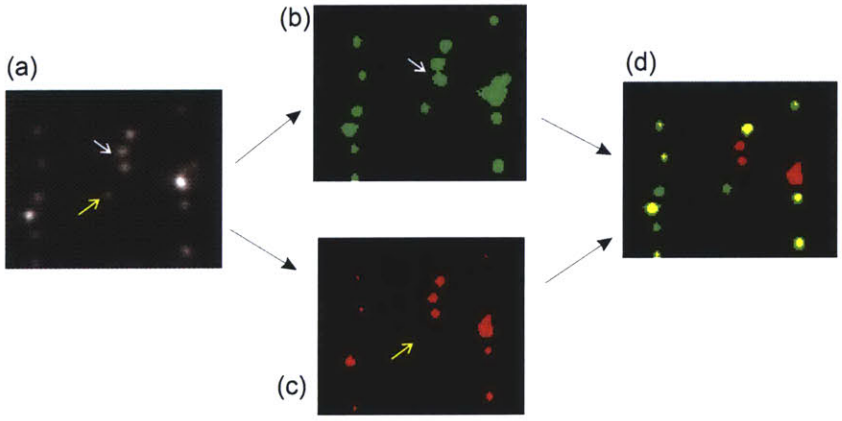

Figure 4-3: Binary image conversion

Two different image conversion methods are used on the original grayscale image (a). The first method (b) uses an absolute threshold which can not identify two close particles (white arrow). The second method (c) uses compressed local peaks, which fails to find dim particles (yellow arrow). By combining the two methods (d), particles can be found more accurately.

The third function of the program is to quantify the particles in the binary image. It first used the *bwlabel* command to label connected objects in the binary image, and then used the *regionprops* command to measure a set of properties for each labeled object. By doing this, I acquired the number of objects in one image and the pixel number of each object. Ideally, one object represents one particle. However, if particles physically touch each other, then the algorithm can not distinguish them as individuals and they will be defined as one big object in the binary image. To identify those indistinguishable objects, the program can automatically calculate the mean particle size of the image and detect those abnormally sized objects. The algorithm will then sort them out and count the actual number of the particles by dividing the object's area by the area of one bead.

4.2.2 Image Processing Validation

To test the reliability of the program versus experimental results, I used the program to measure several samples of known bead concentrations ranging from 1e6 to 1e8 beads/ml. The sample was prepared by diluting the original bead solution (~1e10 beads/ml) with DI water and then measuring with a hemacytometer to acquire the concentration. To prepare the experiment, I flowed the sample solution into the device without an applied voltage. After the entire channel was filled with solution, the flow was stopped and the output of the channel is plugged. To make sure all the particles are on the same focus plane, I turn on the DEP force to trap the beads to the electrode surface (Figure 4-4a). After trapping the particles, the program was run in order to analyze the image taken along the channel and counted the number of beads in each picture. The expected number of beads in each picture can be obtained by multiplying the sample concentration by the volume of the channel covered by the image.

The program exhibited the ability to measure the number of beads with less than 20% error. However, when the concentration became higher than 5e7 bead/ml, the error increased up to 37%. This is because the trapped beads pile up when the bead concentration increases, making the observed bead concentration lower than the actual amount when observed from an overhead view. To overcome this problem, I found that turning the DEP off allows the trapped beads to diffuse slightly, aiding in the observation (Figure 4-4b). The beads dispersed due to Brownian motion and reduced the

overlapping problem. Figure 4-4 shows the measurement result with DEP on and DEP off. At high concentration, the DEP-off method exhibited a more accurate measurement.

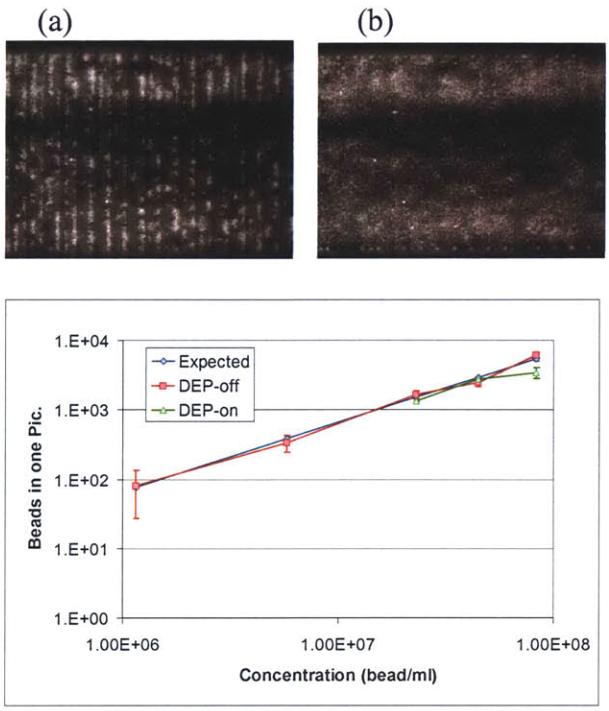

Figure 4-4: Experimental calibration with binary algorithm

Pictures of particles in the channel when DEP is on (a) and off (b). As shown in the graph, the algorithm works better when DEP is off, since particles are not forced to clump together on the electrodes.

4.3 Experiment

I build up an experimental protocol to test my device by using the materials, tools and setups described in previous sections. I used this protocol for all of my experiments in order to maintain the same conditions in every experiment.

The protocol starts with sample preparation. I diluted the original bead solution (~1e10 beads/ml) with DI water to about the desired concentration. The exact concentration of the prepared samples was then acquired by measuring the sample with a hemacytometer. I wanted the concentrated sample to be within the range that I can measure with my visual counting program. According to the simulation, a 100 μl input

sample will be concentrated on average by ~6× in the device and greater than 6× in the beginning of the channel. Therefore, the optimal input sample concentration is 1e5~1e6 beads/ml. Due to the reasons such as water evaporation, bead sedimentation, fluorescent photobleaching, the sample concentration and intensity vary with stored time. To ensure the sample quality, I prepared fresh samples for each experiment

Prior to performing the experiment, I first set the 6-port valve to the loading mode and flushed the channel with DI water. Bubbles usually formed in the mixer grooves even under a very high driving pressure (~2000 μl/min). To eliminate bubbles, I plugged the outlet and increase the pressure inside the channel by pumping the syringe. Because PDMS is porous, when the inner pressure increases, air tends to escape through the PDMS and to the atmosphere making bubbles disappear.

While degassing the channel, I loaded the sample into a 100 μl fixed-volume loading tubing. I then unplugged the output and started the flow at 200 μl/min. I waited for 1 min to let the flow rate stabilize. Next, I applied the voltage to electrodes and turned the 6-port valve to the inject mode to introduce the beads into the channel (Figure 4-5a). During the bead trapping process, I optically monitored the channel with a microscope.

When the full volume of the sample (100 μl) has flowed through the device, I stopped the flow and plugged the outlet again. I then waited for 1 min to make sure the flow was static and then turned off the voltage to let the beads diffuse. The diffusion made the beads easier to observe. After sufficient diffusion time (~20 secs), I took

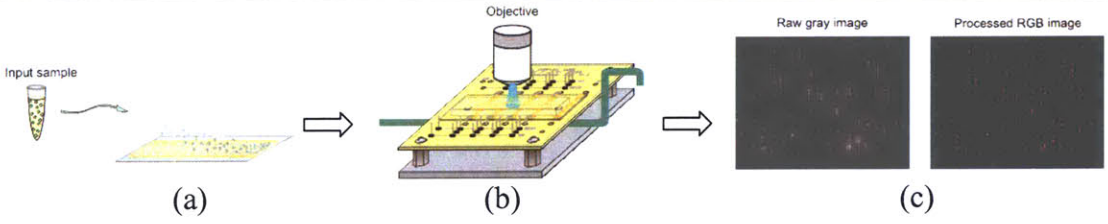

Figure 4-5: Measurement process for device characterization

(a) First, a sample of known concentration of beads is flowed and trapped in the channel by DEP. (b) Second, pictures of the trapped beads are taken. (c) Third, image processing tools are used to analyze the picture and determine the number of trapped beads. The measured concentration is then compared to the known concentration.

pictures along the whole channel (Figure 4-5b), and analyzed the data with the algorithm described previously (Figure 4-5c).

At the end of each experiment, I flow Alconox into the channel to release the trapped beads. Alconox is a kind of anionic detergent which forms a hydrophilic sheath around the particles allowing them to be swept off the surface and to be released. If there are still some residual beads, I detach the fluidic channel and attach Scotch tape (3M, St. Paul, MN) to the electrodes to peel off the remaining beads.

Chapter 5: Result

I characterized the micromixer performance by analyzing trapped bead data from the experiments. I also used COMSOL Multiphysics to simulate the same devices in order to compare the simulations with actual results. In this chapter, I first compare the numerical and experimental trapping results both qualitatively and quantitatively. I then determine the actual micromixer performance from the experimental trapping data.

5.1 Trapped Particle Distribution

Observing the trapped particle distribution is one way to qualitatively and quantitatively characterize the device performance. The trapped particle distribution can be obtained either numerically or experimentally by using the method described in section 2.2 and 4.3, respectively.

5.1.1 Qualitative Results

Inspired by the colored particle tracking method that Kang *et al.* used in [25], I utilized a similar tracking method in the simulation to acquire more distribution information. To mimic the actual experiment, the particles are started randomly in the beginning of the channel and to obtain a steady result, a sufficient amount of particles are required. Figure 5-1 is the relation between the trapped particle percentage and the number of starting particles. Form the error bars of the data points, it shows that the more starting particles, the more stable the result. However, increasing the particle amount increases the simulation time as well. I decided to use ~1000 particles in the simulation since it provides a stable result and also requires a reasonable time (~1 min to calculate the trajectories of 1000 particles). Figure 5-2a illustrates how 1000 colored particles get started at the beginning of the channel. Figure 5-2b shows the top view of the trapped particle distribution which exhibits a distinctive pattern corresponding to the mixing manners, and Figure 5-2c shows the trajectories of two representative particles from both streams moving in 3-D.

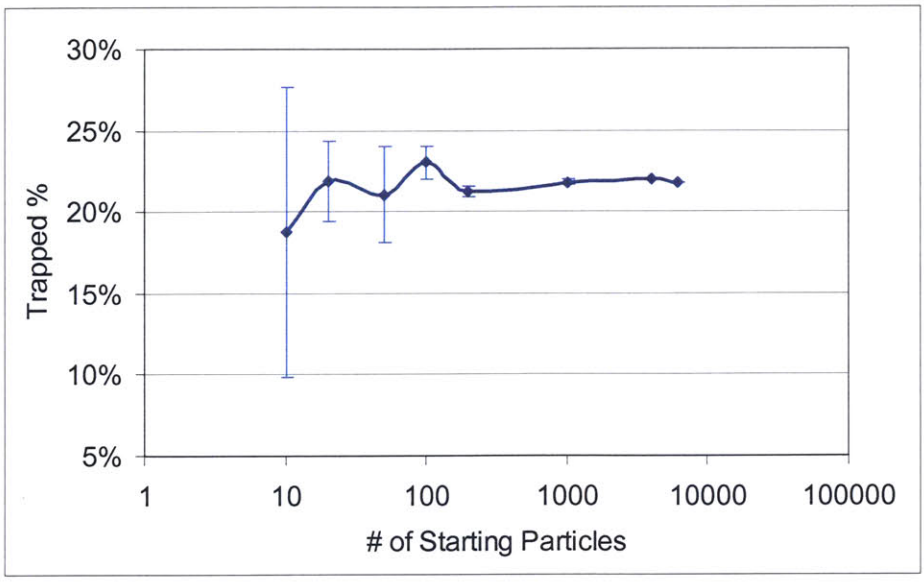

Figure 5-1: The stability of the trapping result versus the number of starting particles

The trapped percentage is defined by the number of trapped particles divided by the total starting particles. Each data point represents the trapping result of 8 simulations. Different amounts of particles are started randomly at the beginning of the channel. As more starting particles are used, the standard deviation of the trapped result gets smaller indicating the result is getting steadier. The parameters used in the simulation: particle diameter 1μm, bead density 100 kg/m^3, media density 1000 kg/m^3, CM factor 0.8, applied voltage 20 V_{pp}, flow rate 200 μl/min, electrode width and spacing 20 μm.

The particles in SGM are distributed evenly and uniformly along the width. On the other hand, in SHM and HM, fewer particles are trapped around the centerline. I believe that the lack of particles in the middle is associated with the shape of the herringbone which lifts particles around the middle of the width (Figure 5-2c, HM and SHM). It is also notable that the trapped position of different color beads is distinct in each mixer. In SGM, pink and yellow beads appear in turn (Figure 5-2b, SGM) because the two streams are twisted and sent to the bottom one at a time (Figure 5-2c, SGM). In HM, beads of the same color remain on the same side since the mixing pattern consists of two individual circles (Figure 5-2b,c, HM). In SHM, the distribution of color beads is random due to the chaotic mixing mechanism (Figure 5-2b,c, SHM).

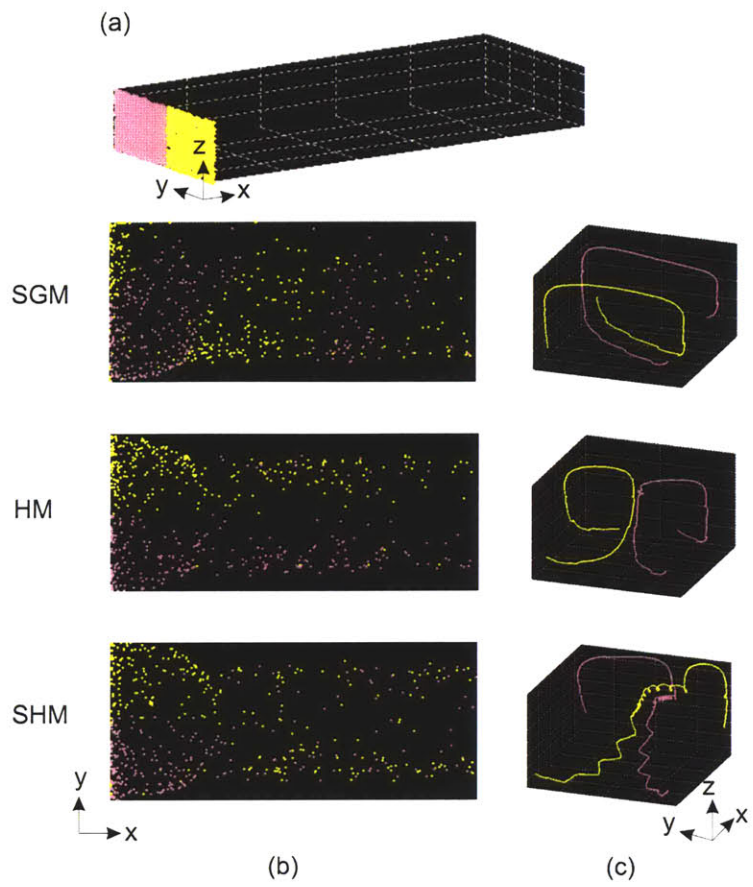

Figure 5-2: Particle distribution and flow streams

(a) Illustration of the starting position of particles. (b) Top view of the trapped beads along the channel. (c) Two representative particle trajectories from each stream. The simulation conditions are the same as those in Figure 5-1

In addition to simulations, experimental measurements with the same condition as in simulation were performed. Although only one kind of bead was used in the experiment, the overall distribution still shows a pattern similar to the simulated pattern. Over 6 experiments, the bead distributions all exhibited a similar pattern. Figure 5-3 shows fluorescent images of the trapped bead distribution obtained from one representative experiment. Obviously, around the centerline, HM and SHM both have a blank strip where few beads are trapped, while SGM does not. Moreover, the trend of the blank strip wiggles around the centerline in SHM. I believe the phenomenon is associated with its asymmetric herringbone grooves.

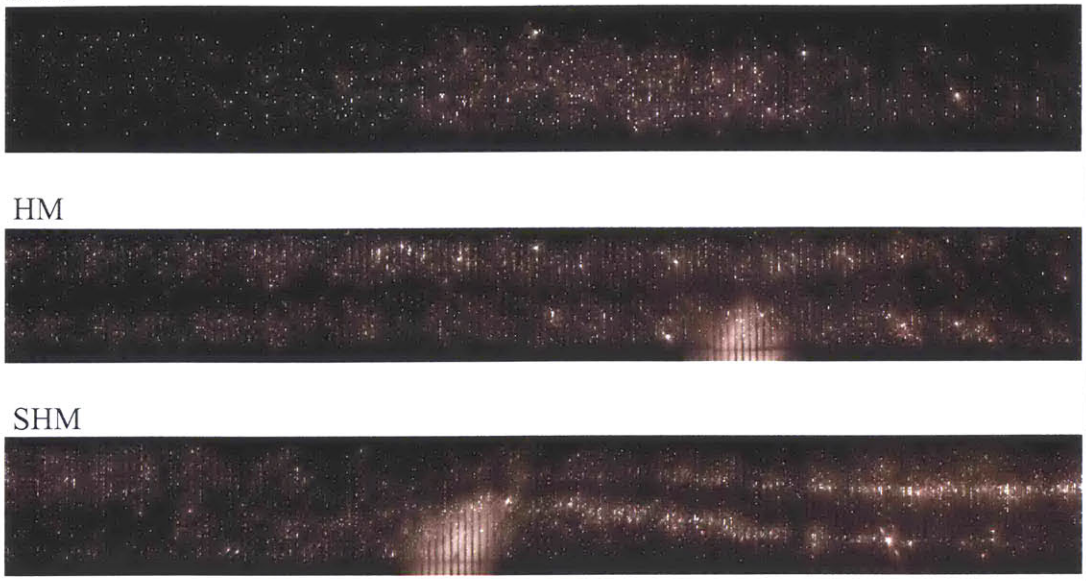

Figure 5-3: Microscope photographs of the trapped bead distribution along the channel

Top view of the trapped bead distribution in SGM, HM and SHM. Beads are trapped evenly and uniformly along the width in SGM. A blank strip where few beads accumulated appears both in HM and SHM.

5.1.2 Quantitative Results

To obtain quantitative experimental results, I performed the experiment described in section 4.3 and counted the number of trapped beads by the visual counting algorithm as described in section 4.2. Figure 5-4 shows the quantitative result. There are 64 images taken along the channel, and each image covers the entire width but only 1/64 of the length of the channel. I performed 6 experiments under the same condition on one device except the input concentration varied from 1e5 to 1e6 bead/ml. The trapping distribution exhibited a constant trend over the 6 experiments. One representative result is shown in Figure 5-4.

At the beginning of the channel, the number of trapped beads in the three different kinds of mixers was similar to that in the smooth channel. Because there were still sufficient beads close to the electrodes, the circulation did not make much difference at

this point. However, in the smooth channel, the number of trapped beads dropped dramatically after a certain distance from the starting point. On the other hand, because of the circulation caused by mixers, in HM, SGM, and SHM, more beads were exposed to the DEP field and trapped along the channel. Particularly in SHM, its chaotic mixing pattern could expose the most beads to the DEP effective region, so the number of trapped beads remained the highest most of the time.

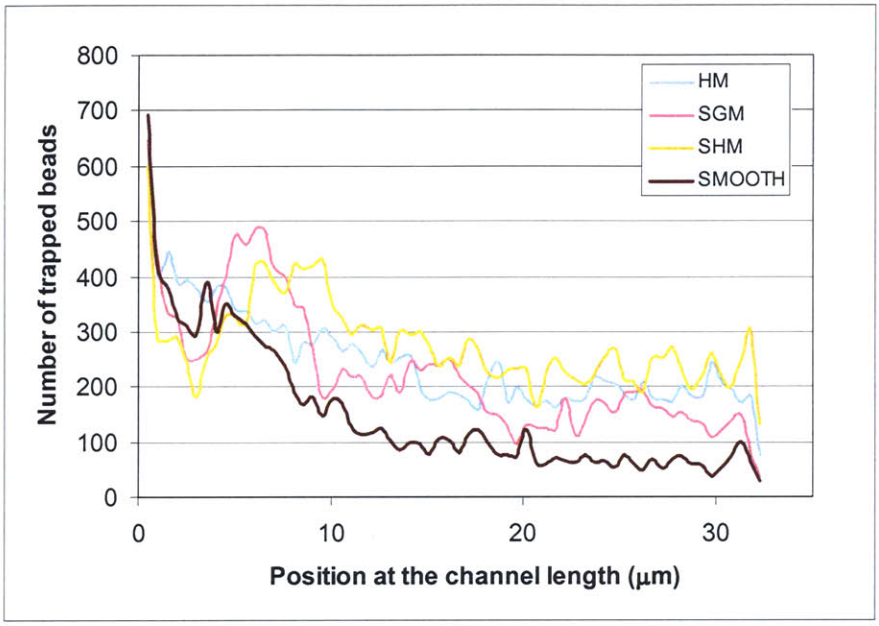

Figure 5-4: Experimental trapped bead number along the channel length

The experiments were performed with a 200 μl/min flow rate and 10 volts. The input sample volume is 100 μl, and the sample concentration is 8.5e5 bead/ml.

5.2 Trapping Enhancement

To examine the efficiency, I repeated the experiment in section 5.1.2 but changed the input sample concentration from 1e5 to 1e6 bead/ml. The results are shown in Figure 5-5, where the trapping efficiency is defined as [total number of beads trapped]/[total number of input beads]. The total number of trapped beads is calculated by integrating the bead distribution as shown in Figure 5-4 and the total number of input beads was calculated from the input concentration multiplied by the channel volume. The input

concentration was measured with a hemacytometer as mentioned in section 4.3. SHM exhibited the greatest trapping enhancement, while the smooth channel always remained the lowest, and other two mixers, SGM and HM, stayed in the middle in performance. Although the performance results may vary from time to time in different experiment runs (standard deviation ~2% which might be caused by the error in the measured input concentration or the fouled electrodes), the relationship among the mixers always remains the same.

The results of the experiment are compared with those of the simulation in Figure 5-6. The simulation accounts for the real dimension of the fabricated device, including the width of electrodes and the aspect ratio of the groove to the channel. The simulation error bar is obtained by repeating the same simulation with particles starting at random points. The results of the experiment are in agreement with those of the simulation to within experimental and simulation error.

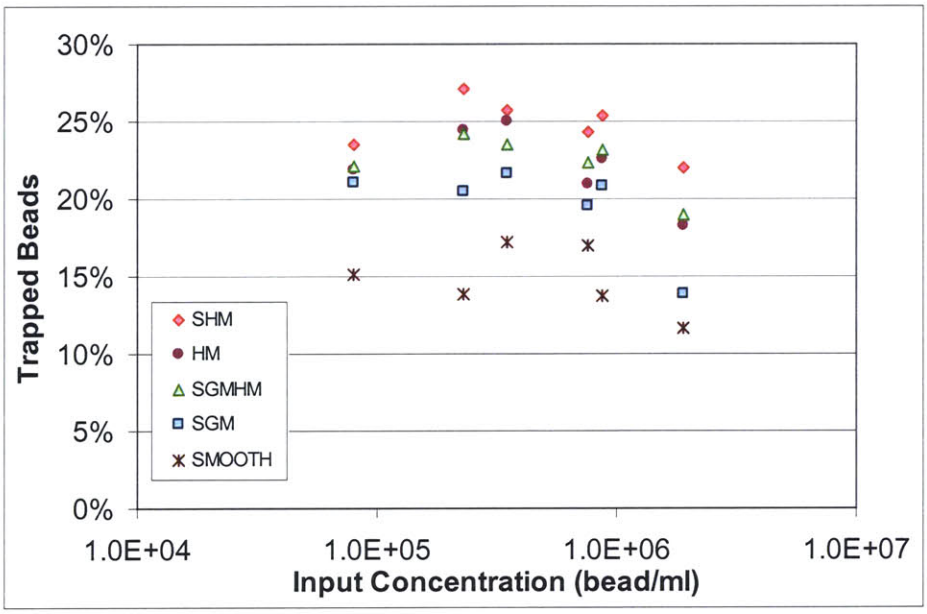

Figure 5-5: Experimental trapping efficiency with varying input concentration

The experiments were performed with 200 μl/min flowrate and 20 volts. The electrode used in the experiments are 20 μm. The input sample volume is 100 μl. Each data point represents one experiment result.

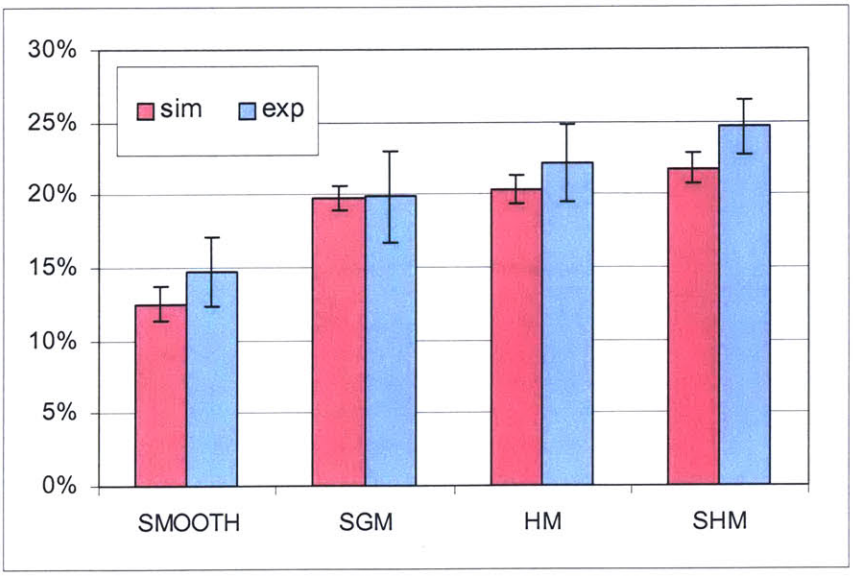

Figure 5-6: Comparison of simulation and experimental trapping efficiency

The dimensions of the fabricated device are: electrode width 16 μm, spacing 24 μm, the groove to channel aspect ration 0.22, 0.23, and 0.25 for SGM, HM and SHM, respectively. The standard deviation of the simulation result is obtained from 5 simulations with particles starting at random initial positions. The experimental result is the integrated data shown in Figure 5-5.

5.3 Combination of Mixers

As presented in the previous section, the mixing circulation of SGM and HM only allows a certain fraction of the particles to go to the electrodes at the bottom of the chamber. In contrast, in the SHM all particles have access to the bottom electrodes because of its chaotic mixing feature. I believe this is the reason why the trapping efficiency of SHM is greater than the other two mixers. I assumed that using a combination of SGM and HM, I might be able to compensate for the poor mixing of either mixer and improve their performance. Therefore, I added a section of HM right after SGM to pull out the particles that remained in the middle of the channel. Figure 5-7 shows a comparison between the trapped beads in a regular SGM and those in a modified mixer SGM+HM. The SGM+HM has a channel filled with slanted grooves in the first half of the channel and herringbone grooves in the second half. When the herringbone grooves are encountered, the number of trapped beads increases dramatically. Over 6

experiments, SGM+HM exhibit a performance better than SGM but still worse than SHM (Figure 5-5).

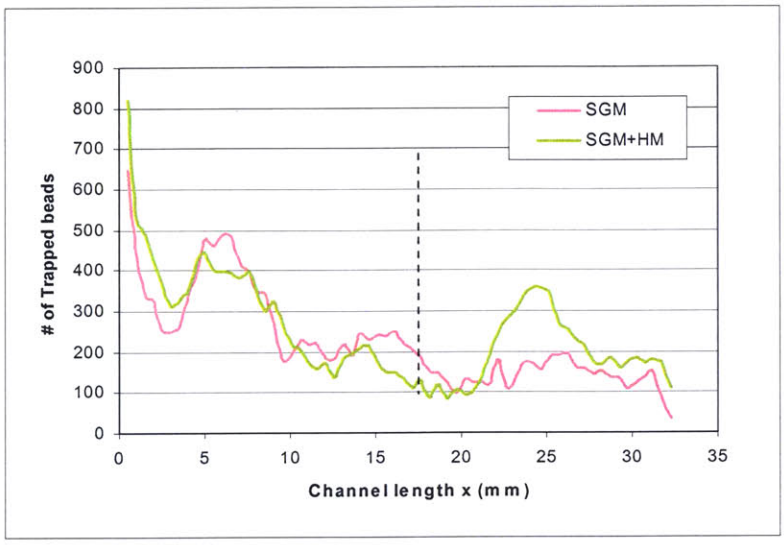

Figure 5-7: Combinational mixer performance

The plot shows the number of trapped beads along two different channels. Before the dash line, both channels are filled with slanted grooves. After the dash line, slanted grooves remain in SGM, but they are replaced by herringbone grooves in SGM+HM. An obvious increase in the number of trapped beads happens in SGM+HM after the dash line.

Chapter 6: Challenges and Future Work

In this chapter, I conclude the work I have done, indicate the challenges I have encountered, and suggest possible directions for the future work. I break the discussion of these three points into four chapter specific sections: simulation, mixer optimization, fabrication and testing. Finally, I discuss the contributions of the work.

6.1 Simulation

The modeling environment I developed is capable of computing the numerical fluid flow field, analytical electric field, and the corresponding forces exerted on the particles in the device. I used the approximation that particles followed the force streamline if the particle is small and thus the system is in quasi-steady state. By taking small enough steps in particle motion, the path of the particle could be calculated directly by the force field. By visualizing the particle trajectory, I was able to determine the mixing mechanism in each mixer and predict the particle trapping both qualitatively and quantitatively.

However, towards comparing the predictions to experimental results, I found that they only met with limited success. The simulation results for each micromixer matched the experimental results with an acceptable error (~3%, based on Figure 5-6), but the simulated difference between the different mixers was not as great as that observed in the experiments. Here I discuss some of the possible ways to improve the simulation to fit the experimental result more accurately.

6.1.1 Resolution for DEP Modeling

When a particle is trapped and immobilized by DEP forces to the electrode, due to the small radius of the particle, the center of the particle is located very close to the electrode surface where the DEP force is less well defined. On the surface of the electrodes, the DEP force exhibits a singularity at the electrode edge. A few microns away from the surface, the singularity is smoothed out but the peak is still narrow. When sampling the DEP force with discrete data points, the resolution becomes important in capturing the narrow peaks. Figure 6-1 shows DEP force in the z direction with varying

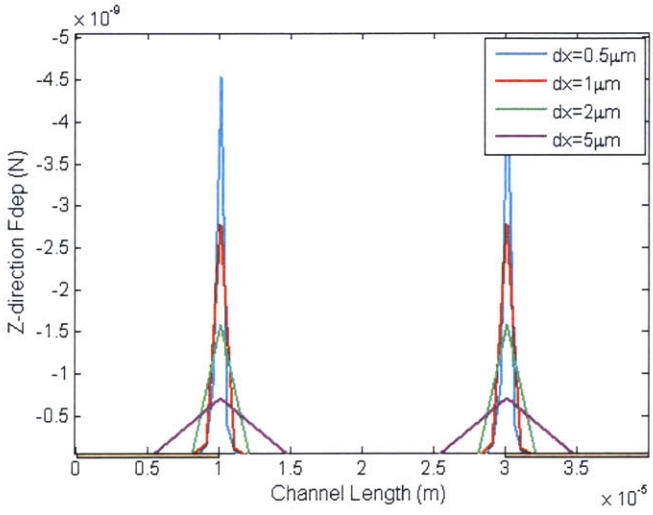

Figure 6-1: Plot of z-directed DEP force

Z-directed DEP force plotted at z = 0.5 μm with varying resolution. The width and spacing of electrode are 20 μm.

sampling interval dx. The smaller the interval, the sharper the sampled DEP force. I have observed that with sharper sampled DEP force, the electrode can hold particles against higher flow rates and thus trap more particles. In my simulation, the minimum resolution was about 1μm due to memory limitations. If the memory space is sufficient, a finer resolution could be used to improve the modeling accuracy.

6.1.2 Shielding Effect

I simplified the simulation by assuming particles were passive and ignored the particle volume. In other words, the simulation did not account for the electrical shielding effect and the volume barrier caused by the accumulated particles on the electrodes. The simulation allowed particles to accumulate at the same spot with an arbitrary amount. On the other hand, in the experiment, the electrode was saturated by accumulated beads so that only a limited amount of beads could be trapped in an area.

To eliminate this discrepancy, one can operate the experiment with a low concentration sample so that the saturation of the electrodes is less significant, or take electrode saturation into account in the simulation. Modifications to the simulation can be achieved by measuring the number of beads which saturate one pair of electrodes, and

based on this information, determine whether or not electrodes still have room to trap particles.

6.2 Mixer Optimization

Since the purpose of the mixers was to enhance the trapping concentration rather than create a uniformly mixed liquid, I examined multiple mixer geometries, some which performed chaotic mixing (SHM), and some which only created very ordered flows (SGM). While the simulation and experiment showed that adding any kind of mixer enhanced the trapping efficiency, it was found that the SHM exhibited the most trapping enhancement. Interestingly, this mixer provided a chaotic rather than an ordered flow pattern. While the ordered flow-based mixers performed worse than the SHM, it was determined that these mixers could be modified to perform more efficient particle trapping by altering flow patterns to force more beads to the bottom of the channel. Two ordered mixers which resulted from this were the HM and the SGM+HM, which both resulted in higher concentration enhancements over SGM. While these modified mixers were able to send more particles to the bottom with their ordered flow patterns, the nature of ordered flows meant that there were always regions near the center of flow vortices which would be incapable of moving particles closer to the electrodes. Therefore, over long mixing lengths, it was still found that the chaotic mixer, SHM, would perform at the highest efficiency over any engineered ordered mixers.

From these results, I conclude that if the mixer geometry can be created with a shorter mixing length or a more chaotic flow pattern, the particle trapping efficiency can be improved. To achieve a shorter mixing length, device dimensions can be changed, such as the aspect ratio between the mixer grooves and the channel height. By applying a stronger mixing force to the chaotic mixer, the probability that particles can reach the electrodes increases. While this approach increases the particle mobility, it is important to note that changing the mixer dimensions too drastically can have adverse effects such as an increase in shear force in both the transverse direction from the mixing pattern and in the axial direction from the decreased channel height. For creating a more chaotic flow pattern, different mixer geometries can be explored, such as a periodic SGM+HM or a W-shaped herringbone mixer geometry. In addition to modifying the roof of the

channel, patterns can also be designed into the sidewalls to aid in particle movement through mixing vortices. All of these designs could potentially increase the concentration efficiency of the system.

6.3 Fabrication

I fabricated the main components of the device: interdigitated electrodes and micromixers with standard MEMS technology. In general, the fabrication process is simple and only needs 3~5 days to fabricate one device. Nevertheless, controlling the uniformity of the SU-8 mold was the most challenging part. The fabricated SU-8 mold had a 10~20% error in height and the half-groove depth varied from 1.8~2.6. The varying half-groove depth affected the mixing performance by changing the mixing length (the length of one mixing cycle). Figure 6-2 shows the exponential relation between the mixing length and the groove aspect ratio.

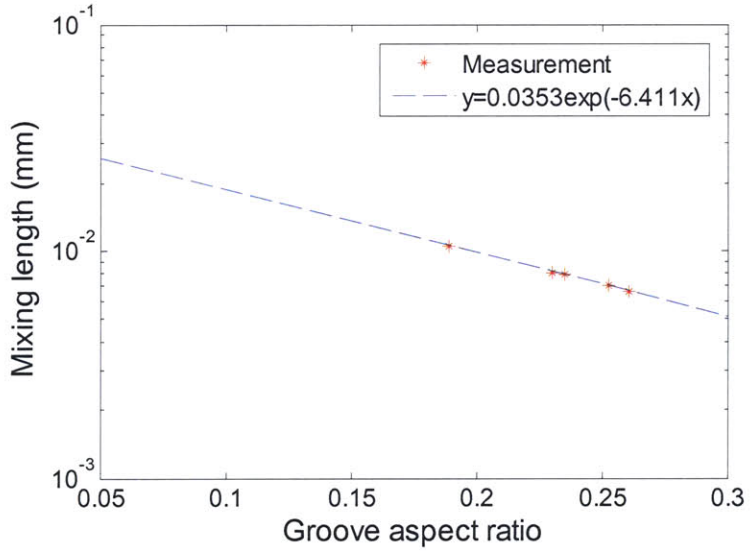

Figure 6-2: Length of SGM to complete one circulation

The length of one mixing period has an exponential relation to the groove aspect ratio α. The dotted line is the mixing length as a function of α, which is obtained from simulation. The red dots are the mixing length corresponding to the actual aspect ratio of fabricated mixers. The channel height is 250 μm and width 500 μm in this case. The mixing length is independent of flow velocity.

To reduce the fabrication error, one can consider other available techniques. For example, using Deep Reactive Ion Etching (DRIE) on silicon wafers is an alternative way to make micro structures for molding PDMS. DRIE has been used to etch deep (~300 μm) and high aspect ratio (>20:1) structures due to its good profile control and low non-uniformity across a wafer of 5% or less [37].

6.4 Testing

I have performed experiments on devices with different micromixers. The experiments were designed to reveal the performance of different micromixers under the same flow rate, applied voltage, and input sample concentration. The developed image counting tool quantified the trapping results and enabled the determination of the trapping efficiency by calculating the percentage of the trapped beads. While the developed tool successfully counted the number of beads in a given sample, it was restricted to situations where the majority of beads were not aggregated. In situations where there was a great deal of bead aggregation, it was hard for the program to distinguish between compacted clumps of beads from single beads. Due to this problem, bead concentrations were determined with the DEP field off so that beads could disperse slightly before imaging. While this fixed the problem of bead aggregation, other problems became more prominent such as beads migrating out of focus, which could affect the imaged bead size and bead intensity.

To improve the measurement of bead concentration from a sample, more detailed calibration can be performed. Since the tool is already capable of determining the locations of aggregated beads, different levels of aggregation can be intensity calibrated to determine a relation between number of aggregated beads and the total aggregate intensity. By adding this functionality to the existing two methods for bead counting, a more accurate measurement of bead concentration can be performed, and concentration measurements could be performed without turning off DEP trapping and waiting for bead dispersal.

6.5 Contributions

I have optimized the micromixer for a DEP-based concentrator by modeling and demonstrating the experimental result. I have established a modeling environment for simulating the particle motion in the device and have also predicted the trapping efficiency numerically. I have developed an experiment method for demonstrating the performance of fabricated devices and comparing the experimental results with the numerical results. For quantifying the experimental results, I have developed an image counting tool to count the number of trapped beads and have determined the trapping efficiency of the device. The optimal mixer among those I have investigated is the Staggered Herringbone Mixer (SHM) which enhanced the trapping efficiency by 1.5× as compared to a smooth channel.

Appendix: Fabrication Process Flow

Starting Materials:

- For electrodes: 150-mm-diameter, 762-μm-thick Pyrex wafers (Bullen Ultrasonics, Eaton, OH)
- For channel (PDMS) patterning: 150-mm-diameter, 650-μm-thick Silicon wafers (WaferNet, Inc., San Jose, CA)

Step	Description	Machine (TRL)	Parameters
Electrode Pattern, on 6" Pyrex wafer			
1	Piranha clean	Acid hood	
2	Dehydration bake	HMDS oven	120°C, 30 mins
3	HMDS	HMDS	Recipe 4
4	Photoresist coat	coater	AZ 5214E image reversal photoresist (3000rpm final speed)
5	Prebake	pre-bake oven	90°C, 30 mins
6	UV expose	EV1	Mask 1
7	Post-expose bake	post-bake oven	95°C, 30 mins
8	UV expose	EV1	Flood (60 sec)
9	Develop, rinse and spin dry	photo-wet-r	AZ 422 developer
10	Metal evaporation	e-beam	100Å Ti, 2000Å Au
11	Liftoff metal	solvent-Au	
12	Protective resist coat	coater	AZ 5214E, 500rmp final speed
13	Bake	Post-bake oven	95°C, 45 mins
14	Dice wafer	Die saw	

Microfluidic Channel Pattern, on 6" Silicon wafer			
1	Dehydration bake	hotplate	200°C, 30mins
2	SU-8 Spin	SU8-spinner	• SU-8 2050 (100 μm thickness): • Dispense ~6ml SU-8 (1ml per inch diameter) • Ramp to 500 rpm at 100 rpm/sec accel and hold for 20 seconds (or until it spreads out) • Ramp to 1680 rpm at 300 rpm/sec and hold for total of 30 seconds
3	Prebake	hotplate	65°C for 5 mins; ramp to 95°C, keep at 95°C for 10 mins. Cool gradually.
4	SU-8 Spin	SU8-spinner	• SU-8 2050 (100 μm thickness): • Dispense ~6ml SU-8 (1ml per inch diameter) • Ramp to 500 rpm at 100 rpm/sec accel and hold for 20 seconds (or until it spreads out) • Ramp to 1680 rpm at 300 rpm/sec and hold for total of 30 seconds
5	Prebake	hotplate	65°C for 4 mins; ramp to 95°C, keep at 95°C for 45 mins (or until not sticky.) Cool gradually.
6	UV expose	EV1	Mask 2, 36 sec
7	Post-expose bake	hotplate	65°C for 1 min; transfer to 95°C for 9 mins, ramp down to ~40°C to cool
8	SU-8 Spin	SU8-spinner	• SU-8 2050 (100 μm thickness): • Dispense ~6ml SU-8 (1ml per inch diameter) • Ramp to 500 rpm at 100 rpm/sec accel and hold for 18 seconds (or until it spreads out) • Ramp to 1680 rpm at 300 rpm/sec and hold for total of 30 seconds
9	Prebake	hotplate	65°C for 5 mins; ramp to 95°C, keep at 95°C for 60 mins (or until not sticky.) Cool gradually.
10	UV expose	EV1	Mask 3, 23 sec
11	Post-expose bake	hotplate	65°C for 1 min; 95°C for 9 mins, rap to 40°C to cool
12	Develop	Solvent-Au	~7-10 mins, visual stop
13	Silylation wafer	EML acid hood	• Put 3-4 drops of HMDS into cup in vacuum jar. • Place wafer(s) against wall of jar. • Close jar, turn on vacuum for 5-10 minutes, then turn vacuum off, let sit for some time (~1 hour). Vent.

References

1. Douglas R. Call, M.K.B., Frank J. Loge, *Detection of bacterial pathogens in environmental samples using DNA microarrays.* Journal of Microbiological Methods, 2003. **53**: p. 235-243.
2. Darwin R. Reyes, D.I., Pierre-Alain Auroux, and Andreas Manz, *Micro Total Analysis Systems. 1. Introduction,Theory, and Technology.* Analytical Chemistry, 2002. **74**: p. 2623-2636.
3. Torsten Vilkner, D.J., and Andreas Manz, *Micro Total Analysis Systems. Recent Developments.* Analytical Chemistry, 2004. **76**: p. 3373-3386.
4. Pierre-Alain Auroux, D.I., Darwin R. Reyes, and Andreas Manz, *Micro Total Analysis Systems. 2. Analytical Standard Operations and Applications.* Analytical Chemistry, 2002. **74**: p. 2637-2652.
5. Lichtenberg, J.V., E.; de Rooij, N. F., *Sample preconcentration by field amplification stacking for microchip-based capillary electrophoresis.* ELECTROPHORESIS, 2001. **22**(2): p. 258-271.
6. Ikuta, K.M., S. Fujisawa, T. Yamada, A., *Micro concentrator with opto-sense micro reactor for biochemical ICchip family. 3D composite structure and experimental verification.* Micro Electro Mechanical Systems, 1999. MEMS '99. Twelfth IEEE International Conference, 1999: p. 376-381.
7. Catherine R. Cabrera, P.Y., *Continuous concentration of bacteria in a microfluidic flow cell using electrokinetic techniques.* ELECTROPHORESIS, 2001: p. 355-362.
8. Blanca H. Lapizco-Encinas, B.A.S., Eric B. Cummings, Yolanda Fintschenko, *Insulator-based dielectrophoresis for the selective concentration and separation of live bacteria in water.* ELECTROPHORESIS, 2004. **25**(10-11): p. 1695-1704.
9. Gadish, N., *A Combined Microfluidic/Dielectriohoretic Microorganism Concentrator*, in *Electrical Science and Engineering*. 2005.
10. Charles L. Asbury, A.H.D., Ger van den Engh, *Trapping of DNA by dielectrophoresis.* ELECTROPHORESIS, 2002. **23**: p. 2658-2666.
11. Muller, R., *A Microfabricated Dielectrophoretic Micro-organism Concentrator*, in *Department of Electrical Engineering and Computer Science*. 2004, MASSACHUSETTS INSTITUTE OF TECHNOLOGY: Cambridge. p. 85.
12. Singh, E.B.C.a.A.K., *Dielectrophoresis in Microchips Containing Arrays of Insulating Posts: Theoretical and Experimental Results.* Analytical Chemistry, 2003. **75**: p. 4724-4731.
13. Barrett, L.M.S., A.J. Singh, A.K. Cummings, E.B. Fiechtner, G.J., *Insulating dielectrophoresis for the continuous separation and concentration of Bacillus subtilis.* Microtechnology in Medicine and Biology, 2005. 3rd IEEE/EMBS Special Topic Conference on: p. 3-4.
14. Guangbin ZHOU, M.I., Junya SUEHIRO and Masanori HARA, *A Dielectrophoretic Filter for Separation and Collection of Fine Particles Suspended in Liquid.* Industry Applications Conference, 2002. 37th IAS Annual Meeting. Conference, 2002. **2**: p. 1404-1411.

15. Morgan, L.C.a.H., *Design and fabrication of travelling wave dielectrophoresis structures.* J. Micromech. Microeng., 2000. **10**: p. 72-79.
16. Pethlg, Y.H.a.R., *Electrode design for negative dielectrophoresis.* Meas. Sci. Technol., 1991. **2**: p. 1142-1146.
17. Joel Voldman, M.L.G., Mehmet Toner, and Martin A. Schmidt, *A Microfabrication-Based Dynamic Array Cytometer.* Analytical Chemistry, 2002. **74**: p. 3984-3990.
18. F. Schönfeld, A., Griebel, R. Konrad, S. Rink, F. Karlsen, *Development of a μ-concentrator Using Dielectrophoretic Forces.* JALA, 2002. **7**(6): p. 130-134.
19. Hong C C, C.J.W.a.A.C.H., *A novel in-plane microfluidic mixer with modified tesla structure.* Lab on a chip, 2004. **74**: p. 4279-4289.
20. Robin H. Liu, M.A.S., Kendra V. Sharp, Michael G. Olsen, Juan G. Santiago, Ronald J. Adrian, Hassan Aref, and David J. Beebe, *Passive Mixing in a Three-Dimensional Serpentine Microchannel.* JOURNAL OF MICROELECTROMECHANICAL SYSTEMS, 2000. **9**: p. 190-197.
21. André Bakker, R.D.L., Elizabeth M. Marshall, *Laminar Flow in Static Mixers with Helical Elements.* 1998.
22. Sung-Jin Park, J.K.K., Junha Park, Seok Chung, Chanil Chung and Jun Keun Chang, *Rapid three-dimensional passive rotation micromixer using the breakup process.* Journal of Micromechanics and Microengineering, 2004. **14**: p. 6-14.
23. Timothy J. Johnson, D.R., and Laurie E. Locascio, *Rapid Microfluidic Mixing.* Analytical Chemistry, 2002. **74**: p. 45-51.
24. Abraham D. Stroock, S.K.W.D., Armand Ajari, Igor Mezić, Howard A.Stone, George M. Whitesides, *Chaotic Mixer for Microchannels.* SCIENCE, 2002. **295**: p. 647-651.
25. Kang, T.G. and T.H. Kwon, *Colored particle tracking method for mixing analysis of chaotic micromixers.* Journal of Micromechanics and Microengineering, 2004. **14**: p. 891-899.
26. McGraw, A.D.S.a.G.J., *Investigation of the staggered herringbone mixer with a simple analytical model.* Phil. Trans. R. Spc. Lond., 2004. **A**(362): p. 971-986.
27. Nguyen, N.T. and Z. Wu, *Micromixer-a review.* Journal of Micromechanics and Microengineering, 2005. **15**: p. R1-R16.
28. Hardt, F.S.n.a.S., *Simulation of Helical Flows in Microchannels.* AIChE, 2004. **50**(4).
29. John Patrick Bennett, C.H.W., *A Computational Study of Mixing Microchannel Flows.* American Physical Society, Annual APS March Meeting 2003, 2003: p. 13.006.
30. Wang, H., et al., *Numerical investigation of mixing in microchannels with patterned grooves.* Journal of Micromechanics and Microengineering, 2003. **13**: p. 801-808.
31. Carolyn R. Kaplan, D.R.M., and Elaine S. Oran, *Towards the Design of Effecient Micromixers.*
32. Chuang Li, T.C., *Simulation and optimization of chaotic micromixer using lattice Boltzmann method.* Sensors and Actuator s B, 2005. **106**: p. 871-877.

33. Dong Eui Chang, S.L., Igor Mezić, *Closed-form solutions in the electrical field analysis for dielectrophoretic and travelling wave inter-digitated electrode arrays.* Journal of PHYSICS D: APPLIED PHYSICS, 2003. **36**: p. 3073-3078.
34. Taff, B.M., *Design and Fabrication of an Addressable MEMS-Based Dielectrophoretic Microparticle Array*, in *ELECTRICAL ENGINEERING AND COMPUTER SCIENCE.* 2004, MASSACHUSETTS INSTITUTE OF TECHNOLGY: MA. p. 116.
35. Vahey, M.D., *A Novel Method for the Contunuous Separation Microorganisms based on Electrical Properties.* 2006, Massachusetts Institute of Technology.
36. Vincent, L., *Morphological Grayscal Reconstruction in Image Analysis: Applications and Efficient Algorithms.* IEEE TRANSACTIONS ON IMAGE PROCESSING, 1993. **2**(2): p. 176-201.
37. A A Ay'on, R.L.B.a.K.S.B., *Deep reactive ion etching: a promising technology for micro- and nanosatellites.* Smart Materials and Structures, 2001. **10**: p. 1135-1144.